Regular Article

Protograph LDPC-Coded Superposition Modulation for MIMO Channels with Triple Mixed-ADC Architectures

Duc A. Hoang[1], Thang N. Le[2], Hieu T. Nguyen[3]

[1] Faculty of Telecommunications, Posts and Telecommunications Institute of Technology, Hanoi, Vietnam
[2] Postgraduate Studies Faculty, Posts and Telecommunications Institute of Technology, Hanoi, Vietnam
[3] Dept. of Science and Industry Systems, Faculty of Technology, Natural Sciences and Maritime Sciences, University of Southeast Norway

Correspondence: Hieu T. Nguyen, hieu.nguyen@usn.no
Communication: received 11 August 2025, revised 03 October 2025, accepted 07 October 2025
Online publication: 08 October 2025, Digital Object Identifier: 10.21553/rev-jec.416

Abstract– **This paper investigates an energy-efficient large-scale multiple-input multiple-output MIMO (LS-MIMO) receiver that integrates a triple mixed-analog-to-digital converter (ADC) architecture with superposition modulation (SM) and protograph-based low-density parity-check (LDPC) coding. The considered receiver employs groups of one-, two-, and five-bit ADCs to reduce front-end cost compared with full-resolution designs, while offering improved performance over a uniform 1-bit baseline in the tested simulations. A double-layer factor-graph detector is developed, and analytical log-likelihood expressions are derived under an additive-quantization-noise model to account for attenuation and quantization effects across ADC tiers. A protograph extrinisic information transfer (PEXIT)-based analysis is adapted to study iterative-decoding thresholds and examine design parameters such as SM weights, protograph matrices, and resolution allocations across various LS-MIMO configurations. Simulation results for representative setups align with the PEXIT predictions and show performance gains for the triple mixed-ADC configuration relative to a uniform 1-bit system. In line with previous findings, equal-weight SM demonstrated competitive performance and, in the tested settings, yielded the lowest thresholds. The proposed analysis framework may be useful for guiding protograph design in systems that combine SM, mixed-resolution ADCs, and LS-MIMO. The 1-, 2-, and 5-bit configuration reflects a practical tradeoff between energy consumption and detection performance, corresponding to realistic base station deployments where only a small subset of antennas can be equipped with higher-resolution converters.**

Keywords– **Large-scale MIMO, Protograph LDPC, Low-Resolution ADC, Triple Mixed-ADCs, Superposition Modulation, PEXIT Analysis**

1 Introduction

The LS-MIMO transmission technique has become an important transmission paradigm for 5G and emerging wireless systems, supporting the increasing demand for high-throughput links in diverse scenarios [1–3]. However, LS-MIMO architectures with hundreds or even thousands of receive antennas face a significant challenge: the high power consumption associated with the large number of radio-frequency (RF) chains [4, 5]. For example, a millimeter-wave LS-MIMO array with 256 RF chains and 512 high-resolution (8–12-bit) ADCs can require a total power draw of around 256 watts [5]. This is because the hardware cost and power usage of ADCs and digital-to-analog converters (DACs) scale linearly with signal bandwidth and, more critically, increase exponentially with converter resolution. One approach to address this issue is to replace high-resolution converters with lower-power, low-resolution counterparts [5–14]. While this inevitably leads to some performance loss in baseband processing—particularly in channel-gain estimation and data detection—the resulting power savings make it a practical option for future LS-MIMO deployments.

This study presents an integrated detection-and-decoding strategy that combines a double-layer factor-graph detector with protograph-based LDPC codes for LS-MIMO systems employing an SM scheme to improve bandwidth efficiency. The receiver front-end uses a triple mixed-ADC architecture with three distinct quantization resolutions to reduce power consumption while maintaining bit-error-rate (BER) performance. In addition, an analytical framework is developed to describe system performance in relation to (i) the LS-MIMO array dimensions, (ii) the LDPC code parameters, (iii) the SM coefficients, and (iv) the allocation of extremely low-, low-, and high-resolution antenna chains in the triple mixed-ADC configuration.

1.1 Related Previous Works

A substantial body of work has examined the impact of coarse quantization and hardware impairments on system performance [9, 11–14]. Nguyen *et al.* proposed learning-based schemes—leveraging either parity-check redundancy or the to-be-decoded payload—to address scenarios in which accurate channel state information (CSI) at the base station is imperfect or unavailable. Their approach demonstrated improved

performance and robustness in LS-MIMO receivers employing low-resolution ADCs [10]. Along similar lines, Gao *et al.* [9] applied deep-learning techniques to channel estimation in mixed-ADC LS-MIMO arrays, where a small subset of antenna elements is equipped with high-resolution converters and the remainder use low-resolution ones. Their method uses the high-resolution observations to help estimate the channels of antennas with coarse quantizers, showing performance gains even in the challenging 1-bit mixed-ADC setting.

Mousavi *et al.* [14] investigated a two-stage signal-detection scheme that combines zero-forcing (ZF) processing with a reduced-complexity maximum-likelihood (ML) search for 1-bit LS-MIMO receivers. This hybrid ZF–ML detector improves detection accuracy compared with conventional ZF while maintaining a computational cost substantially lower than full ML detection. In a related 1-bit-quantized setting with an embedded message-passing channel decoder, Cho *et al.* [13] developed a soft-metric computation method for generating log-likelihood ratios (LLRs), enabling iterative information exchange between the LS-MIMO detector and the decoder to mitigate inter-stream interference. The proposed soft-output architecture achieved better performance than ZF-based counterparts under both perfect and imperfect CSI at the base station. Extending this soft-output approach, Nguyen *et al.* [12] studied coded LS-MIMO systems using few-bit ADCs and protograph LDPC codes, employing joint detection and decoding with parallel-interference cancellation at the receiver. Their results indicate that increasing the number of receive antennas can help offset the performance loss due to low-resolution converters, with 4-bit ADC configurations approaching the performance of high-resolution systems in several LS-MIMO scenarios.

Regarding the theoretical limits—particularly the achievable sum-rate of multi-user MIMO (MU-MIMO) systems with coarse quantization, Fan *et al.* [4] derived a closed-form approximation that accounts for both large-scale and small-scale fading. Consistent with the observations in [11], their results suggest that the rate loss caused by low-resolution ADCs can be alleviated by increasing the number of receive antennas. They also examined energy efficiency, defined to include both transmit power and converter-related power consumption at the antenna array [15], and found that 1-bit and 2-bit ADC architectures offered the most favorable energy-efficiency trade-offs. More recently, Dang *et al.* [16] presented explicit formulas for selecting optimal truncation thresholds for low-resolution ADCs, which improved the achievable uplink sum-rate in MU-MIMO scenarios.

Liu *et al.* [7] studied the impact of signal-detection strategies on the energy efficiency of LS-MIMO receivers with coarse ADCs. Their analysis focused on conventional zero-forcing (ZF) detection and an enhanced version, ZF with successive interference cancellation (ZF-SIC). Assuming identical target rates for all users, they derived closed-form power-allocation rules to maximise energy efficiency. In a related study, Dai *et al.* [8] investigated the achievable rates of full-duplex LS-MIMO links—both uplink and downlink—under low-resolution quantisation. Their results indicate that applying appropriate power-scaling laws, along with increasing the number of antennas at the base station, can help mitigate interference and noise. By contrast, increasing converter resolution alone yields only modest throughput improvements while incurring significant cost and power penalties. Overall, these studies suggest that low-resolution ADC architectures can offer a practical option for energy-efficient LS-MIMO deployments.

Recent research has shown increasing interest in mixed-resolution ADC architectures as a potential approach to addressing the energy and complexity challenges in LS-MIMO systems. Liu *et al.* [17] examined the secrecy performance of cell-free LS-MIMO with mixed-ADC/DAC configurations in the presence of multiple eavesdroppers, showing that carefully designed hybrid quantization can improve physical-layer security. In the radar domain, Wang *et al.* [18] presented a pulse-modulated continuous-wave (PMCW) MIMO radar with mixed-ADCs, enabling efficient angle-Doppler imaging while lowering hardware cost. For extra-large MIMO systems operating in the near field, Liu *et al.* [19] proposed a mixed-ADC architecture designed to support massive access by balancing quantization resolution and system performance.

In the context of intelligent reflecting surface (IRS)-assisted mmWave communications, Hu *et al.* [20] and Chen *et al.* [21] proposed channel estimation algorithms designed to be robust against the nonlinear distortions introduced by low-resolution ADCs. Similarly, Gao *et al.* [22] investigated improved signal detection and estimation methods for mmWave systems equipped with mixed-ADC hardware. Elgabli *et al.* [23] showed that combining multi-bit and one-bit ADCs in uplink LS-MIMO can provide a favorable balance between performance and cost, while Zhao *et al.* [24] developed a robust detection scheme for multi-user signals in mixed-ADC LS-MIMO. Collectively, these studies highlight the practicality of mixed-ADC designs for a range of applications and motivate further investigation of coding and modulation techniques under hybrid quantization constraints.

Previous studies on mixed-ADC LS-MIMO architectures have often focused primarily on information-theoretic analyses, typically assuming random, infinitely long codebooks and thus not accounting for practical implementation constraints. As a result, relatively few works have examined performance using specific, practically deployable families of error-correcting codes. A notable example is the work by Vu *et al.* [12], which evaluated protograph LDPC codes in LS-MIMO systems equipped solely with uniformly low-resolution converters. Protograph LDPC codes generate full-scale parity-check matrices by "lifting" compact base graphs, offering strong error-correction capability alongside inherent rate adaptability and relatively low decoding complexity [25].

In 5G New Radio, protograph LDPC codes serve as the primary channel-coding scheme, with their

structure designed to support a wide range of block lengths and code rates, addressing the diverse requirements of enhanced Mobile Broadband (eMBB) and Ultra-Reliable Low-Latency Communications (URLLC). Looking ahead to 6G, the flexibility and high spectral-efficiency potential of protograph LDPC codes make them promising for data-intensive applications such as holographic telepresence and intelligent machine-to-machine networking [26]. These attributes position protograph-based LDPC schemes as strong candidates for next-generation wireless systems that must meet increasingly stringent reliability and latency requirements. In view of the elevated error rates associated with low-resolution-quantized receivers, researchers have explored joint detection-and-decoding approaches to improve the reliability of LS-MIMO links [27]. Within this research direction, protograph LDPC codes—known for their near-capacity performance and relatively low decoding complexity—have been studied over LS-MIMO channels equipped with coarse ADCs. In addition, extrinsic-information-transfer (EXIT) chart methods have been applied to design and evaluate belief-propagation-based detectors for such LS-MIMO scenarios [28].

The SM technique is a non-bijective signalling method in which multiple binary antipodal symbols are linearly combined according to predefined weighting coefficients. The process begins by demultiplexing a serial bitstream into several parallel branches; each bit is then mapped to an antipodal value from $\{+1, -1\}$. These symbols are scaled by complex-valued weights—often real-valued in one-dimensional constellations—and coherently summed to produce a single complex-valued symbol for transmission [29].

Previous studies have identified several advantages of the SM technique, particularly its potential to improve spectral efficiency. One notable example is the multi-layer superposition modulation (MLSM) framework, based on multiple-slope-keying chirp-spread spectrum (MSK-CSS), which has been developed to increase the throughput of LoRa waveforms in Internet-of-Things (IoT) applications [30]. By assigning distinct modulation factors to each layer, MLSM can embed additional information within a single symbol interval. Furthermore, the layered structure offers a controllable balance between data rate and BER performance, as adjusting the number of superposed layers provides a systematic means of managing this trade-off [30].

Another advantage of superposition modulation is its ability to approach channel capacity on additive-white-Gaussian-noise (AWGN) channels without requiring explicit signal-shaping mechanisms. By the central limit theorem, when a sufficiently large number of independent antipodal symbols are superimposed, the in-phase and quadrature components tend toward Gaussian distributions. This implicit Gaussianisation provides a passive shaping gain that can move the scheme closer to channel capacity [29].

The SM scheme can also offer improved power efficiency compared with conventional bijective constellations (e.g., amplitude-shift keying, ASK) at the same spectral efficiency, as the increased minimum Euclidean distance between neighbouring signal points leads to an inherent "compression" gain. This, in turn, can enable reduced receiver complexity. For instance, under a posteriori probability (APP) detection, the Bahl–Cocke–Jelinek–Raviv (BCJR) algorithm can implement an SM scheme with lower computational cost than bijective mappings. However, the complexity of optimal maximum-a-posteriori (MAP) detection for an SM scheme still grows exponentially with the number of bits per symbol, motivating interest in near-optimal alternatives such as the PDA-GA detector [29, 31].

The SM technique is naturally suited to multi-user and cooperative communication frameworks, allowing terminals to combine their own payloads with relayed information from partner nodes and thereby obtain diversity gains. Coding strategies such as braid coding leverage this feature to enable progressive cooperation in multi-source, single-destination networks [29, 32–34]. When superposition signalling is combined with advanced error-control schemes—such as LDPC or turbo codes—and supported by iterative receiver processing, notable performance improvements have been reported. In particular, repetition coding—typically inefficient over Gaussian channels—can become beneficial in the context of the SM technique, as its redundancy helps reduce the ambiguities associated with the scheme's non-bijective mapping [29, 30, 35].

While the SM scheme offers inherent advantages over conventional constellations: (i) higher spectral efficiency by embedding multiple streams per symbol, (ii) shaping gain that brings its distribution closer to Gaussian capacity-achieving signals, and (iii) improved power efficiency due to increased minimum Euclidean distance between constellation points, the linear decomposition of higher-order modulation system into standard binary-modulated system helps reduce the complexity significantly.

In this work, we focus on triple mixed-ADC LS-MIMO configurations, in which three distinct resolution levels-extremely low, low, and high-are employed with the aim of improving receiver performance while keeping power consumption and complexity relatively low. We also develop a theoretical framework based on an extrinsic information exchange algorithm to characterise the performance of the proposed mixed-ADC system when the channel coding stage uses capacity-approaching yet computationally efficient protograph LDPC schemes. In practice, 1–2 bit ADCs are attractive due to their energy efficiency, while 5-bit ADCs can approximate full-resolution performance at much lower cost. This motivates our study of a triple mixed-ADC architecture (1-, 2-, and 5-bit), which mirrors practical large-scale base station scenarios that must balance cost, power, and performance.

1.2 Contributions

While existing studies have examined either uniformly quantized or dual mixed-ADC architectures, the case of triple mixed-ADCs has not been systematically

studied. Moreover, prior works rarely integrate such architectures with protograph LDPC coding and the SM scheme in a unified analysis framework. Hence, this work investigates LS-MIMO links that integrate an SM technique, protograph LDPC coding, and a triple mixed-ADC front end. The main contributions are as follows:

- **Triple mixed-ADC architecture for LS-MIMO:** While most prior works consider either uniform low-resolution ADCs or dual mixed-ADC setups, our work introduces and analyzes a three-tier resolution design (1-, 2-, and 5-bit). This configuration more closely reflects practical deployment constraints, where only a small fraction of antennas can use higher-resolution converters.
- **Joint double-layer detection and decoding:** We develop a joint detection-and-decoding architecture tailored specifically for triple mixed-ADCs. This graph explicitly models information exchange across extremely low-, low-, and higher-resolution subgraphs, which has not been addressed in prior dual mixed-ADC studies.
- **PEXIT framework extension:** We extend PEXIT analysis beyond its conventional use in uniform or dual mixed-ADC systems. Our variant incorporates cross-resolution interactions within the joint MIMO–LDPC detection-decoding graph. This allows us to predict iterative decoding thresholds that align closely with simulation results, providing a reliable design tool.
- **Design insights:** Our analysis shows, for example, that an equal-weight SM scheme consistently achieves lower thresholds across resolution splits, and that triple mixed-ADCs approach the performance of 5-bit systems with far fewer high-resolution converters. These insights are not apparent from dual mixed-ADC analyses alone.

1.3 Outline

The remainder of this paper is organized as follows. Section 2 presents the protograph LDPC-coded communication system model, which employs a triple mixed-ADC LS-MIMO transmission scheme with an SM scheme. Section 3 describes the high-to-low modulation model conversion and the joint LS-MIMO signal detection and channel decoding algorithm based on a double-layer factor graph. Section 4 introduces the triple mixed-ADC LS-MIMO PEXIT algorithm, used to analyse the performance of protograph LDPC codes and high-order SM schemes in LS-MIMO systems with mixed-ADCs. Analytical results obtained from this method are discussed in Section 5, while Section 6 presents simulation results to validate the analysis. Finally, Section 7 offers concluding remarks.

2 System Model

We consider an LS-MIMO communication system with N_t transmit antennas and N_r receive antennas. Let $\mathbf{b}$ denote an input bit sequence of length K_c. This sequence is first encoded using a protograph LDPC encoder, producing a coded bit stream $\mathbf{c}$ of length N_c. The coded sequence $\mathbf{c}$ is then converted from serial to parallel form in blocks of size $2G$, where $G = \log_2(M)/2$ and M denotes the modulation order.

Within each $2G$-bit block, G bits are mapped to the in-phase (I) component and the remaining G bits to the quadrature (Q) component. In the SM framework, each bit $U_{I,l}$, for $l = 1, 2, \ldots, G$, is modulated using binary phase-shift keying (BPSK) and scaled by a superposition factor $\alpha_{I,l}$, subject to

$$\sum_{l=1}^{G} \alpha_{I,l}^2 = 0.5.$$

A similar procedure is applied to the G bits on the quadrature branch, where each bit is scaled by $\alpha_{Q,l}$, for $l = 1, 2, \ldots, G$, satisfying

$$\sum_{l=1}^{G} \alpha_{Q,l}^2 = 0.5.$$

The overall system model is illustrated in Figure 1. The M-ary SM symbols are then processed by a LS-MIMO encoder implemented using the V-BLAST scheme. Each of the N_t transmit antennas sends a distinct modulated symbol, resulting in N_t parallel data streams. These signals propagate through the LS-MIMO channel and are received by an array of N_r antennas.

The LS-MIMO channel is modelled as

$$\mathbf{R} = \mathbf{H}\mathbf{X} + \mathbf{W}, \tag{1}$$

where

- $\mathbf{X} \in \mathbb{C}^{N_t \times 1}$ is the transmitted symbol vector,
- $\mathbf{H} \in \mathbb{C}^{N_r \times N_t}$ is the channel matrix,
- $\mathbf{W} \in \mathbb{C}^{N_r \times 1}$ is the additive white Gaussian noise (AWGN) vector, assumed to have zero mean and variance N_0.

Without loss of generality, suppose that the modulated symbol $S[m]$ (for $m = 1, 2, \ldots, N_t$) is directly mapped to the corresponding entry $X[m]$ in the LS-MIMO codeword $\mathbf{X}$. The average symbol energy, $E_s = \mathbb{E}\left[\|\mathbf{X}\|^2\right]$, is assumed to be normalized to 1.

We assume that the channel coefficients $H[n, m]$, which form the entries of the matrix $\mathbf{H}$, are drawn independently from a circularly symmetric complex Gaussian distribution with zero mean and unit variance, i.e., $\mathcal{CN}(0, 1)$. Perfect channel state information (CSI) is assumed to be available at the receiver but not at the transmitter. In this work, perfect CSI is assumed at the receiver for tractability. In practice, quantization distortion complicates channel estimation, especially for 1- and 2-bit ADCs, and robust strategies are needed to mitigate this issue. Finally, the received signal vector is given by

$$\mathbf{R} = [R[1],\, R[2],\, \ldots,\, R[N_r]]^{\mathsf{T}},$$

where $R[n]$ is the signal at the n-th receive antenna.

By employing the SM scheme illustrated in Figure 1,

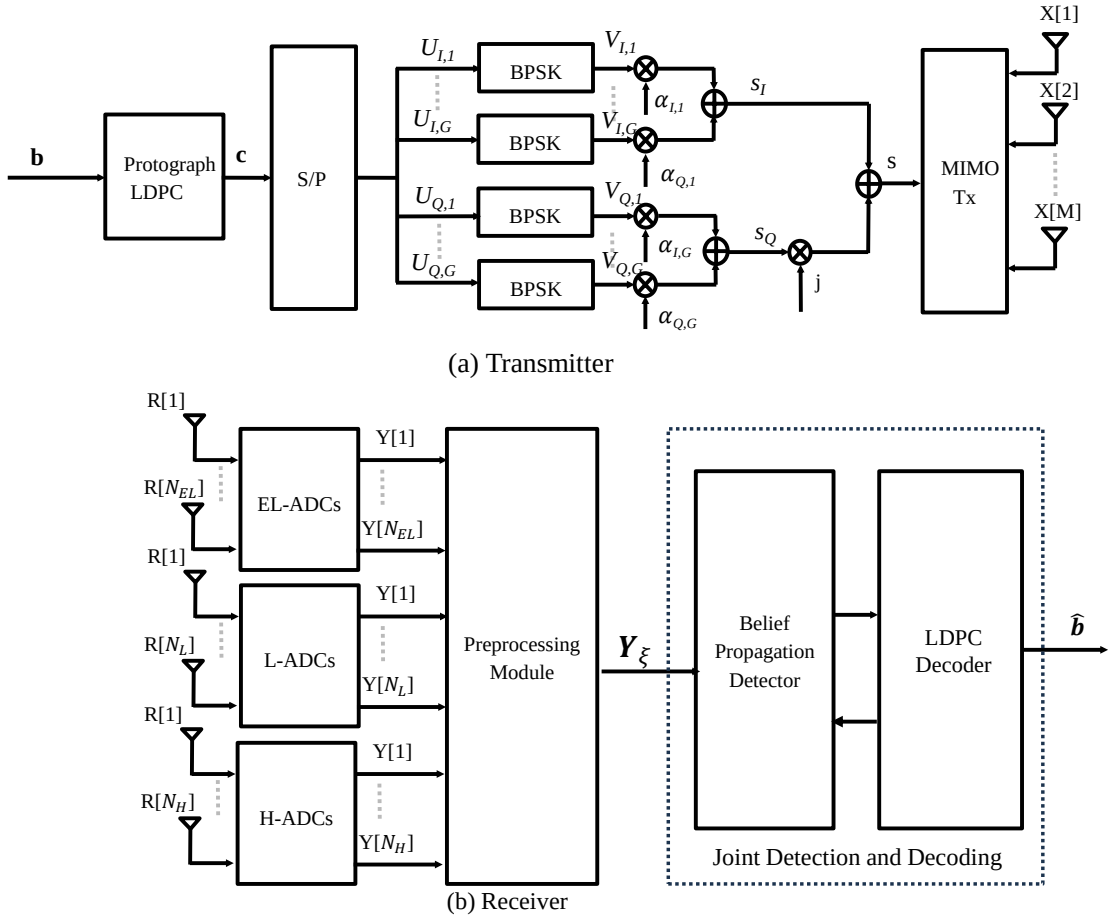

Figure 1. Block diagram of the transceiver in a protograph LDPC-coded MIMO communication system with low-resolution ADCs and the SM technique.

the transmitted symbol $X[m]$ can be written as

$$X[m] = \sum_{l=1}^{G} \alpha_{I,l}\, V_{I,l}[m] \; + \; j \sum_{l=1}^{G} \alpha_{Q,l}\, V_{Q,l}[m], \qquad (2)$$

where $\alpha_{I,l}$ and $\alpha_{Q,l}$ represent the superposition (power) allocation factors for the in-phase and quadrature components, respectively, and $V_{I,l}[m]$ and $V_{Q,l}[m]$ are the BPSK-modulated symbols on each branch. Here, j denotes the imaginary unit.

In this work, we consider three types of ADCs: extremely low-resolution (one-bit) ADCs, low-resolution (two-bit) ADCs, and higher-resolution (five-bit) ADCs, as illustrated in Figure 1. The design focuses on 1- and 2-bit ADCs, which have been reported to offer favourable energy–efficiency trade-offs in prior studies [4]. For the higher-resolution group, five-bit ADCs are used in place of conventional full-resolution devices, based on the findings in [27] that five-bit ADCs can achieve performance comparable to that of full-resolution converters.

The received signal vector $\mathbf{R}$ is divided into three sub-vectors: $\mathbf{R}_{\mathrm{EL}}$ of length N_{EL}, $\mathbf{R}_{\mathrm{L}}$ of length N_{L}, and $\mathbf{R}_{\mathrm{H}}$ of length $N_{\mathrm{H}} = N_r - N_{\mathrm{L}} - N_{\mathrm{EL}}$. These correspond to the signals captured by the extremely low-resolution, low-resolution, and high-resolution antenna groups, respectively. Accordingly, the received vector $\mathbf{R}$ can be expressed as

$$\begin{aligned} \mathbf{R}_{EL} &= \mathbf{H}_{EL}\mathbf{X} + \mathbf{W}_{EL} \\ \mathbf{R}_{L} &= \mathbf{H}_{L}\mathbf{X} + \mathbf{W}_{L} \\ \mathbf{R}_{H} &= \mathbf{H}_{H}\mathbf{X} + \mathbf{W}_{H} \end{aligned} \qquad (3)$$

Here, $\mathbf{H}_{\mathrm{EL}} \in \mathbb{C}^{N_{\mathrm{EL}} \times N_t}$, $\mathbf{H}_{\mathrm{L}} \in \mathbb{C}^{N_{\mathrm{L}} \times N_t}$, and $\mathbf{H}_{\mathrm{H}} \in \mathbb{C}^{N_{\mathrm{H}} \times N_t}$ denote the channel matrices corresponding to the extremely low-, low-, and high-resolution antenna groups, respectively. Similarly, $\mathbf{W}_{\mathrm{EL}} \in \mathbb{C}^{N_{\mathrm{EL}} \times 1}$, $\mathbf{W}_{\mathrm{L}} \in \mathbb{C}^{N_{\mathrm{L}} \times 1}$, and $\mathbf{W}_{\mathrm{H}} \in \mathbb{C}^{N_{\mathrm{H}} \times 1}$ represents the additive white Gaussian noise (AWGN) vectors for each group.

The sub-vector $\mathbf{R}_{\mathrm{EL}}$ is processed by $2N_{\mathrm{EL}}$ pairs of extremely low-resolution ADCs (one-bit in this work), while $\mathbf{R}_{\mathrm{L}}$ is passed through $2N_{\mathrm{L}}$ pairs of low-resolution ADCs (two-bit). The remaining sub-vector $\mathbf{R}_{\mathrm{H}}$ is processed by $2N_{\mathrm{H}}$ pairs of high-resolution ADCs (five-bit in this study), following the findings in [12] that a five-bit ADC configuration can achieve performance close to that of a full-resolution system.

3 Receiver Design

3.1 Analog-to-Digital Conversion Model

Let $Q(\cdot)$ denote the quantization function. The relationship between the input and output of the Q_{EL}-bit

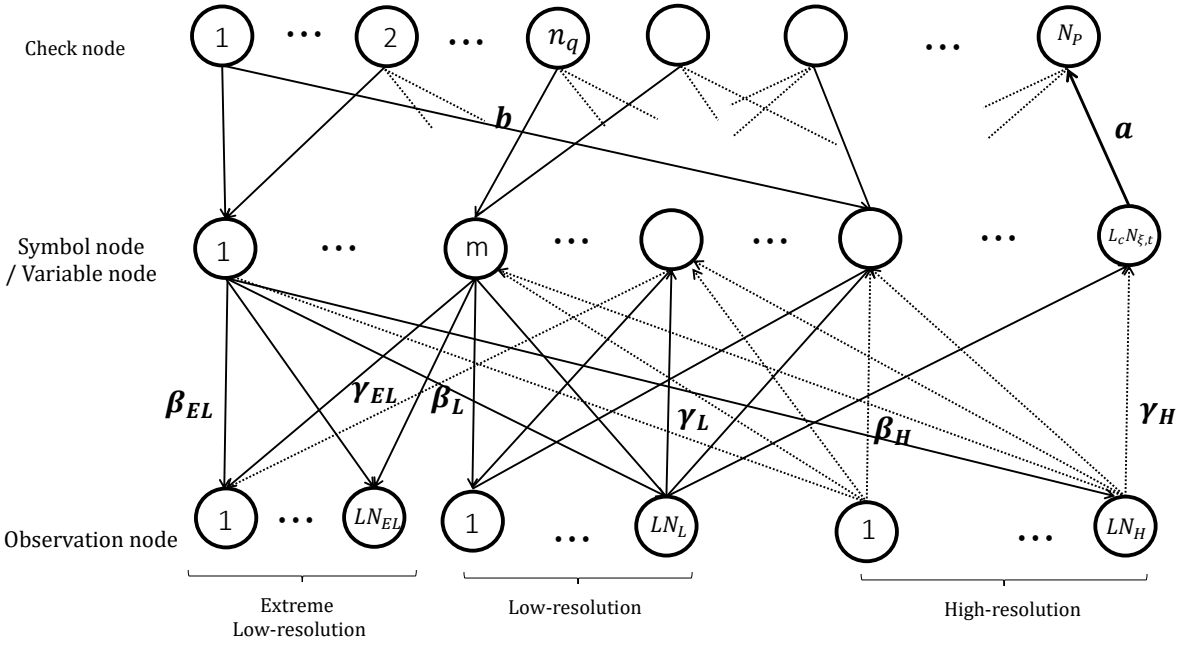

Figure 2. Double-layer factor graph for a joint detection-and-decoding receiver with triple mixed-ADC architecture.

ADC is given by

$$\mathbf{Y}_{\mathrm{EL}} = Q(\mathbf{R}_{\mathrm{EL,re}}) + jQ(\mathbf{R}_{\mathrm{EL,im}}), \tag{4}$$

where $\mathbf{R}_{\mathrm{EL,re}}$ and $\mathbf{R}_{\mathrm{EL,im}}$ denote the real and imaginary parts of the received signal $\mathbf{R}_{\mathrm{EL}}$, respectively.

Similarly, the relationship between the input and output of the Q_{L}-bit ADC is given by

$$\mathbf{Y}_{\mathrm{L}} = Q(\mathbf{R}_{\mathrm{L,re}}) + jQ(\mathbf{R}_{\mathrm{L,im}}), \tag{5}$$

where $\mathbf{R}_{\mathrm{L,re}}$ and $\mathbf{R}_{\mathrm{L,im}}$ represent the real and imaginary components of $\mathbf{R}_{\mathrm{L}}$. Finally, the relationship between the input and output of the Q_{H}-bit ADC is given by

$$\mathbf{Y}_{\mathrm{H}} = Q(\mathbf{R}_{\mathrm{H,re}}) + jQ(\mathbf{R}_{\mathrm{H,im}}), \tag{6}$$

where $\mathbf{R}_{\mathrm{H,re}}$ and $\mathbf{R}_{\mathrm{H,im}}$ denote the real and imaginary parts of the received signal $\mathbf{R}_{\mathrm{H}}$, respectively. Furthermore, the quantizer function Q in this paper operates on a scalar basis, meaning each vector element is quantized independently.

By adopting the additive quantization noise model (AQNM) for LS-MIMO systems with low-resolution ADCs [4, 36], the effect of quantization is modelled as an additional noise term added to the received signal. Under the AQNM framework, the relationship between the quantizer input and output in (4), (5), and (6) is expressed as [4]:

$$\begin{aligned} \mathbf{Y}_{\mathrm{EL}} &= \varphi_{\mathrm{EL}}\,\mathbf{R}_{\mathrm{EL}} + \mathbf{W}_{\mathrm{EL},\Phi}, \\ \mathbf{Y}_{\mathrm{L}} &= \varphi_{\mathrm{L}}\,\mathbf{R}_{\mathrm{L}} + \mathbf{W}_{\mathrm{L},\Phi}, \\ \mathbf{Y}_{\mathrm{H}} &= \varphi_{\mathrm{H}}\,\mathbf{R}_{\mathrm{H}} + \mathbf{W}_{\mathrm{H},\Phi}, \end{aligned} \tag{7}$$

where φ_{EL}, φ_{L}, and φ_{H} are quantizer gain factors, and $\mathbf{W}_{\mathrm{EL},\Phi}$, $\mathbf{W}_{\mathrm{L},\Phi}$, and $\mathbf{W}_{\mathrm{H},\Phi}$ denote the corresponding additive quantization noise vectors. $\varphi_{\mathrm{EL}} = 1 - \rho_{\mathrm{EL}}$, with ρ_{EL} representing the inverse of the signal-to-quantization-noise ratio for the one-bit ADCs. Likewise, $\varphi_{\mathrm{L}} = 1 - \rho_{\mathrm{L}}$ and ρ_{L} is the inverse of the signal-to-quantization-noise ratio for the two-bit ADCs. Finally, $\varphi_{\mathrm{H}} = 1 - \rho_{\mathrm{H}}$, where ρ_{H} is the inverse of the signal-to-quantization-noise ratio for the five-bit ADCs. The vectors $\mathbf{W}_{\mathrm{EL},\Phi}$, $\mathbf{W}_{\mathrm{L},\Phi}$, and $\mathbf{W}_{\mathrm{H},\Phi}$ are the additive Gaussian noise components, which are assumed to be uncorrelated with $\mathbf{R}_{\mathrm{EL}}$, $\mathbf{R}_{\mathrm{L}}$, and $\mathbf{R}_{\mathrm{H}}$, respectively.

In this work, we employ uniform quantizers [37], though the following analysis can also be extended to non-uniform quantizers. Assuming the channel model in (3), the input signals of the Q_{EL}-bit, Q_{L}-bit, and Q_{H}-bit ADCs (depicted in Figure 1) are continuous random variables with infinite support. Hence, the signals $R_{\mathrm{EL}}[n]$, $R_{\mathrm{L}}[n]$, and $R_{\mathrm{H}}[n]$ are truncated to obtain finite supports within the intervals $[-T_{\mathrm{EL},s}, T_{\mathrm{EL},s}]$, $[-T_{\mathrm{L},s}, T_{\mathrm{L},s}]$, and $[-T_{\mathrm{H},s}, T_{\mathrm{H},s}]$, respectively. The corresponding truncation procedures are mathematically defined as follows:

$$\overline{R_{EL}[n]} = \begin{cases} -T_{EL,s}, & R_{EL}[n] < -T_{EL,s}; \\ R_{EL}[n], & -T_{EL,s} \le R_{EL}[n] \le T_{EL,s}; \\ T_{EL,s}, & R_{EL}[n] > T_{EL,s}. \end{cases} \tag{7}$$

$$\overline{R_{L}[n]} = \begin{cases} -T_{L,s}, & R_{L}[n] < -T_{L,s}; \\ R_{L}[n], & -T_{L,s} \le R_{L}[n] \le T_{L,s}; \\ T_{L,s}, & R_{L}[n] > T_{L,s}. \end{cases} \tag{8}$$

and

$$\overline{R_{H}[n]} = \begin{cases} -T_{H,s}, & R_{H}[n] < -T_{H,s}; \\ R_{H}[n], & -T_{H,s} \le R_{H}[n] \le T_{H,s}; \\ T_{H,s}, & R_{H}[n] > T_{H,s}. \end{cases} \tag{9}$$

where $\overline{R}_{\mathrm{EL}}[n]$, $\overline{R}_{\mathrm{L}}[n]$, and $\overline{R}_{\mathrm{H}}[n]$ denote the truncated versions of the received signals $R_{\mathrm{EL}}[n]$, $R_{\mathrm{L}}[n]$, and

$R_{\mathrm{H}}[n]$, respectively. The optimal values of $T_{\mathrm{EL},s}$, $T_{\mathrm{L},s}$, and $T_{\mathrm{H},s}$ depend on both the probability density function of the input and the number of quantization levels [38]. In [27], Dang *et al.* derived the expressions for determining these optimal truncation limits and the corresponding performance metrics φ_{EL}, φ_{L}, and φ_{H} for various resolution levels, which are summarized in Table I.

Table I
Optimal Values of $T_\xi, \xi \in \{EL, L, H\}$ for Different ADC Resolution Levels

Resolution	1	2	3	4	5
T_ξ	1.669	2.0912	2.4613	2.7909	3.0285
φ_ξ	0.6261	0.8796	0.9628	0.9885	0.9936

3.2 M-ary SM to Binary Modulation Model Conversion

In this module, the higher-order modulation is effectively mapped to an equivalent BPSK format, allowing the belief propagation detection algorithm to operate on the double Tanner graph [12, 28]. This strategy highlights a crucial benefit of the SM scheme in LS-MIMO systems with high-order constellations, as it reduces the detector complexity for the LS-MIMO signal.

To start, we represent the LS-MIMO transmit symbol $X[m]$ for the m-th antenna in its complex form, separating the in-phase component $X_I[m]$ from the quadrature component $X_Q[m]$:

$$X[m] = X_I[m] + j\, X_Q[m], \tag{8}$$

where

$$X_I[m] = \sum_{l=1}^{G} \alpha_{I,l}\, V_{I,l}[m] \tag{9}$$

and

$$X_Q[m] = \sum_{l=1}^{G} \alpha_{Q,l}\, V_{Q,l}[m]. \tag{10}$$

We have

$$\mathbf{Y}_{\xi,I} = \varphi_\xi \begin{bmatrix} \mathbf{H}_{\xi,I} & -\mathbf{H}_{\xi,Q} \end{bmatrix} \begin{bmatrix} \mathbf{X}_I \\ \mathbf{X}_Q \end{bmatrix} + \varphi_\xi \mathbf{W}_I + \mathbf{W}_{\xi,I},$$

and

$$\mathbf{Y}_{\xi,Q} = \varphi_\xi \begin{bmatrix} \mathbf{H}_{\xi,Q} & \mathbf{H}_{\xi,I} \end{bmatrix} \begin{bmatrix} \mathbf{X}_I \\ \mathbf{X}_Q \end{bmatrix} + \varphi_\xi \mathbf{W}_Q + \mathbf{W}_{\xi,Q},$$

where

$$\mathbf{X}_I = [X_I[1], X_I[2], \cdots, X_I[N_t]]^T,$$
$$\mathbf{X}_Q = [X_Q[1], X_Q[2], \cdots, X_Q[N_t]]^T,$$

and

$$\xi \in \{EL, L, H\}.$$

Let

$$\mathbf{Y}_\xi = \begin{bmatrix} \mathbf{Y}_{\xi,I} \\ \mathbf{Y}_{\xi,Q} \end{bmatrix},$$

we can rewrite

$$\mathbf{Y}_\xi = \varphi_\xi \begin{bmatrix} \mathbf{H}_{\xi,I} & -\mathbf{H}_{\xi,Q} \\ \mathbf{H}_{\xi,Q} & \mathbf{H}_{\xi,I} \end{bmatrix} \begin{bmatrix} \mathbf{X}_I \\ \mathbf{X}_Q \end{bmatrix} + \begin{bmatrix} \varphi \mathbf{W}_I + \mathbf{W}_{\xi,I} \\ \varphi \mathbf{W}_Q + \mathbf{W}_{\xi,Q} \end{bmatrix},$$

with

$$\mathbf{X}_I[m] = \begin{bmatrix} \alpha_{I,1}, & \alpha_{I,2}, & \ldots, & \alpha_{I,G} \end{bmatrix} \underbrace{\begin{bmatrix} V_{I,1}[m] \\ V_{I,2}[m] \\ \vdots \\ V_{I,G}[m] \end{bmatrix}}_{\mathbf{V}_I[m]} \tag{11}$$

$$\mathbf{X}_Q[m] = \begin{bmatrix} \alpha_{Q,1}, & \alpha_{Q,2}, & \ldots, & \alpha_{Q,G} \end{bmatrix} \underbrace{\begin{bmatrix} V_{Q,1}[m] \\ V_{Q,2}[m] \\ \vdots \\ V_{Q,G}[m] \end{bmatrix}}_{\mathbf{V}_Q[m]}. \tag{12}$$

A concise representation of the transmitted LS-MIMO symbol is given by:

$$\begin{bmatrix} \mathbf{X}_I \\ \mathbf{X}_Q \end{bmatrix} = \begin{bmatrix} \boldsymbol{\alpha}_I & \mathbf{0} \\ \mathbf{0} & \boldsymbol{\alpha}_Q \end{bmatrix} \begin{bmatrix} \mathbf{V}_I \\ \mathbf{V}_Q \end{bmatrix} \tag{13}$$

Here, $\boldsymbol{\alpha}_R$ and $\boldsymbol{\alpha}_I$, both of size $N_t \times G$, contain the superposition coefficients associated with the in-phase and quadrature channels, respectively.

$$\boldsymbol{\alpha}_I = \begin{bmatrix} \alpha_{I,1} & \alpha_{I,2} & \cdots & \alpha_{I,G} \\ \vdots & \vdots & \ddots & \vdots \\ \alpha_{I,1} & \alpha_{I,2} & \cdots & \alpha_{I,G} \end{bmatrix}$$

$$\boldsymbol{\alpha}_Q = \begin{bmatrix} \alpha_{Q,1} & \alpha_{Q,2} & \cdots & \alpha_{Q,G} \\ \vdots & \vdots & \ddots & \vdots \\ \alpha_{Q,1} & \alpha_{Q,2} & \cdots & \alpha_{Q,G} \end{bmatrix}$$

And, $\mathbf{0}$ is the all-zero matrix of size $M \times G$.

$$\mathbf{Y}_\xi = \varphi_\xi \begin{bmatrix} \mathbf{H}_{\xi,I} & -\mathbf{H}_{\xi,Q} \\ \mathbf{H}_{\xi,Q} & \mathbf{H}_{\xi,I} \end{bmatrix} \begin{bmatrix} \boldsymbol{\alpha}_I & \mathbf{0} \\ \mathbf{0} & \boldsymbol{\alpha}_Q \end{bmatrix} \begin{bmatrix} \mathbf{V}_I \\ \mathbf{V}_Q \end{bmatrix} + \begin{bmatrix} \varphi_\xi \mathbf{W}_I + \mathbf{W}_{\xi,I} \\ \varphi_\xi \mathbf{W}_Q + \mathbf{W}_{\xi,Q} \end{bmatrix} \tag{14}$$

or

$$\mathbf{Y}_\xi = \varphi_\xi\, \mathbf{H}_\xi\, \mathbf{V}_\xi + \mathbf{W}_\xi \tag{15}$$

with

$$\mathbf{H}_\xi = \begin{bmatrix} \mathbf{H}_{\xi,I} & -\mathbf{H}_{\xi,Q} \\ \mathbf{H}_{\xi,Q} & \mathbf{H}_{\xi,I} \end{bmatrix} \begin{bmatrix} \boldsymbol{\alpha}_I & \mathbf{0} \\ \mathbf{0} & \boldsymbol{\alpha}_I \end{bmatrix} \tag{16}$$

and

$$\mathbf{V}_\xi = \begin{bmatrix} \mathbf{V}_I \\ \mathbf{V}_Q \end{bmatrix} \tag{17}$$

By definition, the vector $\mathbf{V}_\xi$ contains $2 \times N_t \times G$ entries, each drawn from a BPSK constellation $\{-1, +1\}$.

3.3 Joint Detection and Decoding

When the number of antennas escalates to tens or hundreds, standard MIMO detection methods—such as zero-forcing, minimum mean square error (MMSE) filtering, sphere decoding, and maximum likelihood detection—become computationally intractable [39, 40]. Consequently, message-passing algorithms emerge as a promising alternative [28]. However, most existing message-passing approaches are crafted for high-resolution LS-MIMO systems and cannot be directly ex-

tended to LS-MIMO configurations with low-resolution ADCs. This limitation arises from the extra quantization noise and the altered input signal amplitude. In this section, we develop an LS-MIMO detector based on a Tanner graph [41] tailored for the triple mixed-ADC receiver.

As shown in Figure 2, the detection graph for recovering the transmitted bits comprises two node types: observation nodes and symbol nodes. For an LS-MIMO setting of size $N_t \times N_r$, there are N_r observation nodes (representing N_r receive antennas) and $N_{\xi,t} = 2 \times G \times N_t$ binary symbol nodes. Unlike single low-resolution or dual mixed-ADC systems, the observation nodes here are partitioned into three subsets.

The first subset consists of N_{EL} extremely low-resolution observation nodes employing one-bit ADCs, while the second subset comprises N_{L} low-resolution nodes using two-bit ADCs. The remaining subset consists of N_{H} higher-resolution observation nodes with five-bit ADCs. Owing to the broadcast nature of radio transmissions, the extremely low-resolution, low-resolution, and higher-resolution nodes are all fully connected to the symbol nodes. As a result, the reliability information from the higher-resolution and low-resolution nodes propagates to the extremely low-resolution nodes through the $N_{\xi,t}$ symbol nodes after each iteration. This structure intuitively illustrates how a small number of higher-resolution antennas can enhance the overall performance of a mixed-ADC system.

In the iterative joint detection and decoding algorithm, five distinct message types are exchanged over the graph:

- $L_{\gamma,EL}[n_{EL}, m]$: the message passed from the n_{EL}-th observation node to the m-th symbol node.
- $L_{\gamma,L}[n_L, m]$: the message passed from the n_L-th observation node to the m-th symbol node.
- $L_{\gamma,H}[n_H, m]$: the message passed from the n_H-th observation node to the m-th symbol node.
- $L_a[n_p, n_q]$: the message passed from the n_p-th variable node to the n_q-th check node.
- $L_b[n_q, n_p]$: the message passed from the n_q-th check node to the n_p-th variable node.
- $L_{\beta,EL}[m, n_{EL}]$: the message passed from the m-th symbol node to the n_{EL}-th observation node.
- $L_{\beta,L}[m, n_L]$: the message passed from the m-th symbol node to the n_L-th observation node.
- $L_{\beta,H}[m, n_H]$: the message passed from the m-th symbol node to the n_H-th observation node.
- $L_\Gamma[m]$: the *a posteriori* log-likelihood ratio (LLR) of the symbol $V_\xi[m]$.

In the following, we describe the workings of the message-passing joint detection and decoding receiver, which includes a soft symbol cancellation mechanism.

3.3.1 Message Passed From Observation Nodes To Symbol Nodes: The received signal at the n-th observation node is given as

$$\begin{aligned} Y_\xi[n,m] &= \varphi_\xi \sum_{m=1}^{N_{t,\xi}} H_\xi[n,m]V_\xi[m] + W_\xi[m] \\ &= \varphi_\xi H_\xi[n,m]V_\xi[m] + \\ &\underbrace{\varphi_\xi \sum_{t=1,t\neq m}^{N_{t,\xi}} H_\xi[n,t]V_\xi[t]}_{\text{Interference}} + W_\xi[m], \end{aligned} \tag{18}$$

where $N_{t,\xi} = 2 \times N_t \times G$ and $\xi \in \{\mathrm{EL}, \mathrm{L}, \mathrm{H}\}$.

In contrast to the unquantized (high-resolution) system, the received signal at the n-th antenna for $V_\xi[m]$ is subjected to an extra noise term (quantization noise) and is also attenuated by a factor φ_ξ stemming from the quantization process.

In this work, the parallel interference cancellation technique [39] is employed to remove inter-substream interference in (18). The soft symbol is first estimated using the extrinsic message conveyed from the m-th symbol node to the n_ξ-th observation node. Let $\hat{V}_\xi[n_\xi, m]$ denote the soft symbol derived from the message passed from the n_ξ-th observation node to the m-th symbol node. For the BPSK modulation scheme, the soft symbol can be written as

$$\hat{V}_\xi[n_\xi, m] = \tanh\left(\frac{L_\beta[m, n_\xi]}{2}\right), \tag{19}$$

where $L_\beta[m, n_\xi]$ is the extrinsic message passed from the m-th symbol node to the n_ξ-th observation node. We assume that $L_\beta[m, n_\xi], \forall n = 1, 2, \cdots, L_c N_\xi$, $\forall m = 1, 2, \cdots, L_c N_{t,\xi}$ are uncorrelated and satisfies the consistency condition [42].

The soft symbol in (19) is then used to suppress the interference at the n-th observation node for the m-th transmitted symbol $V_\xi[m]$ as follows

$$\hat{Y}_\xi[n_\xi, m] = Y_\xi[n_\xi, m] \; - \; \varphi_\xi \sum_{t=1,t\neq m}^{N_{t,\xi}} H_\xi[n_\xi, t]\, \hat{V}_\xi[n_\xi, t], \tag{20}$$

where $\hat{Y}_\xi[n_\xi, m]$ represents the received signal for $V_\xi[m]$ at the n_ξ-th observation node after the interference cancellation step.

In general, the soft symbol $\hat{V}_\xi[n_\xi, m]$ provides only an approximate estimate of the transmitted symbol $V_\xi[m]$. As a result, residual interference remains in $\hat{Y}_\xi[n_\xi, m]$ following interference cancellation. Let $Z_\xi[n_\xi, m]$ represent this residual interference plus noise. Then, we have

$$\begin{aligned} Z_\xi[n_\xi, m] = \varphi_\xi \sum_{t=1,t\neq m}^{N_{t,\xi}} H_\xi[n_\xi, t](V_\xi[n_\xi, t] - \hat{V}_\xi[n_\xi, t]) \\ + W_\xi[n_\xi]. \end{aligned} \tag{21}$$

We can now rewrite $\hat{Y}_\xi[n_\xi, m]$ as below

$$\hat{Y}_\xi[n_\xi, m] = \varphi_\xi H_\xi[n_\xi, m]V_\xi[m] + Z_\xi[n_\xi, m]. \tag{22}$$

By treating the residual interference as additive Gaussian noise, the power of the combined residual interfer-

ence and noise term $Z_{\xi}[n_{\xi}, m]$ can be calculated as

$$\Psi_{\xi}[n_{\xi}, m] = \varphi_{\xi}^2 \sum_{t=1, t\neq m}^{N_{t,\xi}} |H_{\xi}[n_{\xi}, t]|^2 (1 - |\hat{V}_{\xi}[n_{\xi}, t]|^2) \quad (23)$$
$$+\varphi_{\xi}^2 N_0 + \varphi_{\xi}(1 - \varphi_{\xi}) \left(\sum_{m=1}^{N_{t,\xi}} |H_{\xi}[n_{\xi}, m]|^2 + N_0 \right).$$

The log-likelihood ratio (LLR) transmitted from the n_{ξ}-th observation node to the m-th variable node is given by

$$L_{\gamma}[n_{\xi}, m] = \ln \frac{\Pr(\hat{Y}_{\xi}[n_{\xi}, m] \mid \mathbf{H}_{\xi}, V_{\xi}[m] = +1)}{\Pr(\hat{Y}_{\xi}[n_{\xi}, m] \mid \mathbf{H}_{\xi}, V_{\xi}[m] = -1)}$$
$$= \frac{4\varphi_{\xi}}{\Psi_{\xi}[n_{\xi}, m]} \Re(H_{\xi}^*[n_{\xi}, m] \hat{Y}_{\xi}[n_{\xi}, m]). \quad (24)$$

In total, there are N_r messages sent to each symbol node (or transmit symbol). Summing these messages yields what is commonly referred to as the channel message (L_{ch}) in standard message-passing algorithms [43]. In contrast to the expression established in [40], the newly proposed form in (24) incorporates the impact of quantization noise through φ_{ξ} and $\Psi_{\xi}[n_{\xi}, m]$, which are functions of the ADC resolution and the fading channels, as discussed previously. When low-resolution ADCs are used, the factor $4\varphi_{\xi}/\Psi_{\xi}[n_{\xi}, m]$ in (24) becomes smaller since φ_{ξ} is proportional to the ADC resolution, leading to a reduction in the channel message $L_{\gamma}[n_{\xi}, m]$. As a result, the channel decoder performance deteriorates.

3.3.2 Message Passed From Variable Nodes To Check Nodes: Focusing on the n_p-th variable node, it receives two categories of messages: one from the N_r observation nodes in the LS-MIMO detection subgraph, and another from the check nodes in the LDPC decoding subgraph. As a result, the extrinsic message passed from the n_p-th variable node to the n_q-th check node consists of the sum of all messages from the observation nodes and check nodes, excluding the message coming from the n_q-th check node. Consequently, we obtain

$$L_a[n_p, n_q] = \sum_{\xi \in \{EL, L, H\}} \sum_{n_t \in \mathcal{S}_{o,\xi}(n_p)} L_{\gamma,\xi}[n_t, n_p] \quad (25)$$
$$+ \sum_{t \in \mathcal{S}_c(n_p) \setminus n_q} L_b[n_t, n_p],$$

Here, $\mathcal{S}_c(n_p)$ is the set of check nodes that connect to the n_p-th variable node, while $\mathcal{S}_{o,\xi}(n_p), \xi \in \{EL, L, H\}$ denotes the set of observation nodes that connect to the m-th variable node.

In contrast to the traditional PEXIT framework, the sum of observation-node messages on the right-hand side of (25), namely $\sum_{n_t \in \mathcal{S}_{o,\xi}(n_p)} L_{\gamma}[n_t, n_p]$, acts as the channel LLR message. A central postulate in developing the PEXIT algorithm is that this channel LLR message follows a symmetric Gaussian distribution [44]. For the LS-MIMO channel incorporating ADCs, previous work [12] has validated that this Gaussian assumption holds true.

3.3.3 Message Passed From Check Nodes to Variable Nodes: The message passed from the n_q-th check node to the n_p-th variable node follows the standard message-passing algorithm [43], and is given by

$$L_b[n_q, n_p] = \ln \frac{1 - \prod_{n_t \in \mathcal{S}_v(n_q) \setminus n_p} \frac{1 - e^{L_a[n_t, n_q]}}{1 + e^{L_a[n_t, n_q]}}}{1 + \prod_{n_t \in \mathcal{S}_v(n_q) \setminus n_p} \frac{1 - e^{L_a[n_t, n_q]}}{1 + e^{L_a[n_t, n_q]}}}, \quad (26)$$

Here, $\mathcal{S}_v(n_q)$ denotes the set of variable nodes connected to the n_q-th check node. In practice, the computation of $L_b[n_q, n_p]$ may be simplified by leveraging the $\tanh(\cdot)$ function.

3.3.4 Message Passed From Symbol Nodes To Observation Nodes: As described before, the m-th symbol node receives messages from both the observation nodes and the check nodes. The extrinsic message transmitted from the m-th symbol node to the n_{ξ}-th observation node consists of all the messages it acquires, excluding the message from the n_{ξ}-th observation node. Consequently, the message from the m-th variable node to the n_{ξ}-th observation node is given by

$$L_{\beta,\xi}[m, n_{\tau}] = \sum_{\xi \in \{El, L, H\}} \sum_{t \in \mathcal{S}_{o,\xi}(m)} L_{\gamma}[t, m] + \quad (27)$$
$$\sum_{n_t \in \mathcal{S}_c(n_p)} L_b[n_t, n_p] - L_{\gamma,\xi}[n_{\xi}, m],$$

where $\mathcal{S}_{o,\xi}(m)$ and $\mathcal{S}_c(n_p)$ denote the sets of observation nodes and check nodes, respectively, that connect to the m-th symbol node.

3.3.5 A posteriori messages of codeword bits: The posterior LLR for the m-th transmit symbol at the conclusion of each iteration is the combined sum of messages from both the observation nodes and the check nodes, expressed as

$$L_{\Gamma}[m] = \sum_{\xi \in \{EL, L, H\}} \sum_{n \in \mathcal{S}_{o,\xi}(m)} L_{\gamma,\xi}[n_{\xi}, m] + \quad (28)$$
$$\sum_{n_q \in \mathcal{S}_c(n_p)} L_b[n_q, n_p].$$

Next, the *a posteriori* LLR is passed to the hard-decision device to generate the decoded version of the codeword bit, following the rule:

$$\hat{c}[m] = \begin{cases} 0, & L_{\Gamma}[m] > 0; \\ 1, & \text{Otherwise.} \end{cases} \quad (29)$$

where $\hat{c}[m]$ represents the decoded version of $c[m]$. Consequently, the decoded information sequence $\hat{\mathbf{b}}$ is obtained.

The message-passing procedure halts once all check equations are fulfilled or when the prescribed maximum number of iterations is reached. If neither condition is met, the process continues by refreshing messages from the observation nodes as detailed in Subsection 3.3.1.

4 Modified PEXIT Algorithm For Triple-Mixed ADCs

The PEXIT algorithm has long been recognized as a useful tool for evaluating the performance of protograph LDPC codes under a variety of channel models [12, 28, 44, 45]. In [44], it was originally introduced for single-input single-output (SISO) additive white Gaussian noise (AWGN) channels, and was subsequently leveraged to design numerous robust protograph LDPC codes tailored for AWGN channels [46]. Later, it was extended to facilitate the performance analysis of protograph LDPC codes over fading channels [45].

Vu *et al.* noted that earlier PEXIT algorithms could not be directly applied to LS-MIMO scenarios involving joint signal detection and decoding. This limitation motivated the development of the LS-MIMO-PEXIT algorithm, which was subsequently used to design new protograph LDPC codes for LS-MIMO channels. A related variation, targeting LS-MIMO systems with low-resolution ADCs, was proposed by Nguyen *et al.* [12], providing important insights into the impact of low-resolution ADCs on LS-MIMO performance. Although the approach in [12] shares similarities with the method considered here, it is not directly applicable to systems employing mixed-ADCs. In the following section, we introduce a new PEXIT algorithm variant specifically designed for LS-MIMO receivers with mixed-ADCs, integrated into a joint detection-and-decoding framework.

The mutual-information flow for the joint detection-and-decoding receiver is shown in Figure 3 and Figure 4. The depicted protograph is a reduced representation of the double-layer graph in Figure 2. For the purpose of information-flow analysis, the variable nodes and symbol nodes are separated into two distinct entities. These entities are linked through a forward combiner for the forward information flow and a backward combiner for the backward information flow.

The LS-MIMO component of the joint MIMO–LDPC protograph consists of N_{EL} extremely low-resolution observation nodes, N_{L} low-resolution observation nodes, N_{H} high-resolution observation nodes, $N_{\xi,t} = 2N_tG$ symbol nodes, and $N_{\xi,t}N_r$ edges. This structure is replicated Π times (equal to the number of channel uses) to form the LS-MIMO section of the double-layer graph in Figure 2.

The LDPC decoding component of the joint detection-and-decoding graph comprises N_P variable nodes, N_Q check nodes, and a set of edges connecting the variable and check nodes. The edge connections are defined by a proto-matrix $\mathbf{B} \in \mathbb{Z}_{\geq 0}^{N_Q \times N_P}$, where $\mathbf{B}[n_q, n_p]$ denotes the number of parallel edges between the n_q-th check node and the n_p-th variable node.

To construct the LDPC portion of the double-layer graph in Figure 2, we first replicate the LDPC segment of the joint MIMO–LDPC protograph $\lambda = \frac{N_c}{N_P} = \frac{L_c N_{\xi,t}}{N_P}$ times, and then apply a permutation to these λ variable-to-check edge pairs, corresponding to the same edge type of the base protograph [47]. Here, $N_Q = \frac{N_c - K_c}{\lambda} = (1 - R_c)N_P$, where R_c is the coding rate of the LDPC code.

We define nine types of mutual information, corresponding to the nine extrinsic messages in the double-layer graph of Figure 2 for the joint LS-MIMO detection and LDPC protograph decoding, as follows:

- $I_{\gamma_{\mathrm{EL}}}[n_{\mathrm{EL}}, m]$: Extrinsic mutual information between the LLR value $\gamma_{\mathrm{EL}}[n_{\mathrm{EL}}, m]$ sent by the n_{EL}-th *extremely low-resolution* observation node and the m-th corresponding coded bit.
- $I_{\gamma_{\mathrm{L}}}[n_{\mathrm{L}}, m]$: Extrinsic mutual information between the LLR value $\gamma_{\mathrm{L}}[n_{\mathrm{L}}, m]$ sent by the n_{L}-th *low-resolution* observation node and the m-th corresponding coded bit.
- $I_{\gamma_{\mathrm{H}}}[n_{\mathrm{H}}, m]$: Extrinsic mutual information between the LLR value $\gamma_{\mathrm{H}}[n_{\mathrm{H}}, m]$ sent by the n_{H}-th *high-resolution* observation node and the m-th corresponding coded bit.
- $I_a[n_p, n_q]$: Extrinsic mutual information between the LLR value $a[n_p, n_q]$ sent by the n_p-th variable node to the n_q-th check node and the n_p-th corresponding coded bit.
- $I_b[n_q, n_p]$: Extrinsic mutual information between the LLR value $b[n_q, n_p]$ sent by the n_q-th check node to the n_p-th variable node and the n_p-th corresponding coded bit.
- $I_{\beta_{\mathrm{EL}}}[m, n_{\mathrm{EL}}]$: Extrinsic mutual information between the LLR value $\beta_{\mathrm{EL}}[m, n_{\mathrm{EL}}]$ sent by the m-th symbol node to the n_{EL}-th *extremely low-resolution* observation node and the m-th corresponding symbol.
- $I_{\beta_{\mathrm{L}}}[m, n_{\mathrm{L}}]$: Extrinsic mutual information between the LLR value $\beta_{\mathrm{L}}[m, n_{\mathrm{L}}]$ sent by the m-th symbol node to the n_{L}-th *low-resolution* observation node and the m-th corresponding symbol.
- $I_{\beta_{\mathrm{H}}}[m, n_{\mathrm{H}}]$: Extrinsic mutual information between the LLR value $\beta_{\mathrm{H}}[m, n_{\mathrm{H}}]$ sent by the m-th symbol node to the n_{H}-th *high-resolution* observation node and the m-th corresponding symbol.
- $I_{\Gamma}[n_p]$: A posteriori mutual information between the LLR value $\Gamma[n_p]$ and the corresponding codeword bit of the n_p-th variable node.

Moreover, we denote by P_p the punctured label of the n_p-th variable node, which is assigned the value 0 when the n_p-th variable node is punctured (i.e., the corresponding codeword bits are not transmitted) and 1 otherwise.

4.1 Forward Mutual Information Flow

The forward mutual-information flow describes the propagation of extrinsic mutual information from the observation nodes, through the symbol nodes and variable nodes, and finally to the check nodes, as shown in Figure 3. In the following, we derive the mutual-information functions for the forward direction, with particular attention to the interaction between the low-resolution ADC subgraph and the high-resolution ADC subgraph.

4.1.1 Mutual Information From Observation Nodes To Symbol Nodes: The m-th symbol node receives N_{EL}

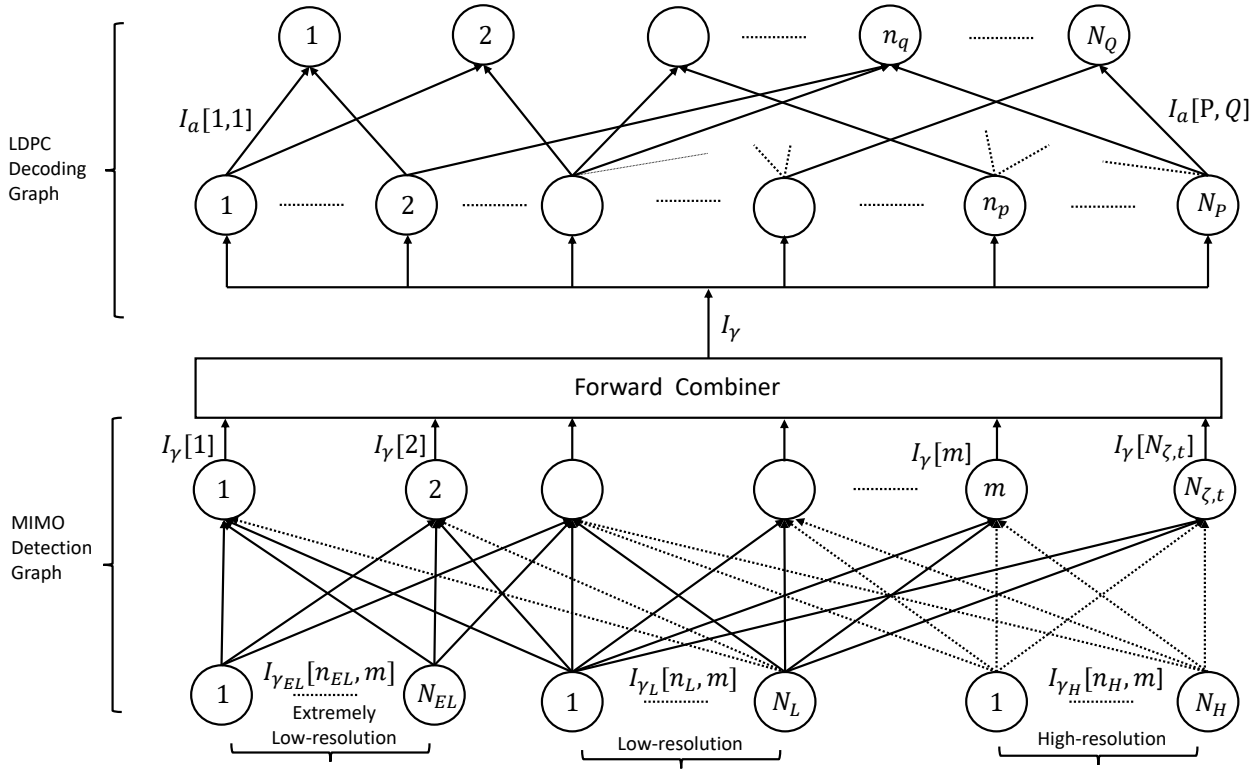

Figure 3. Forward information flow in the proposed triple mixed-ADC LS-MIMO PEXIT framework.

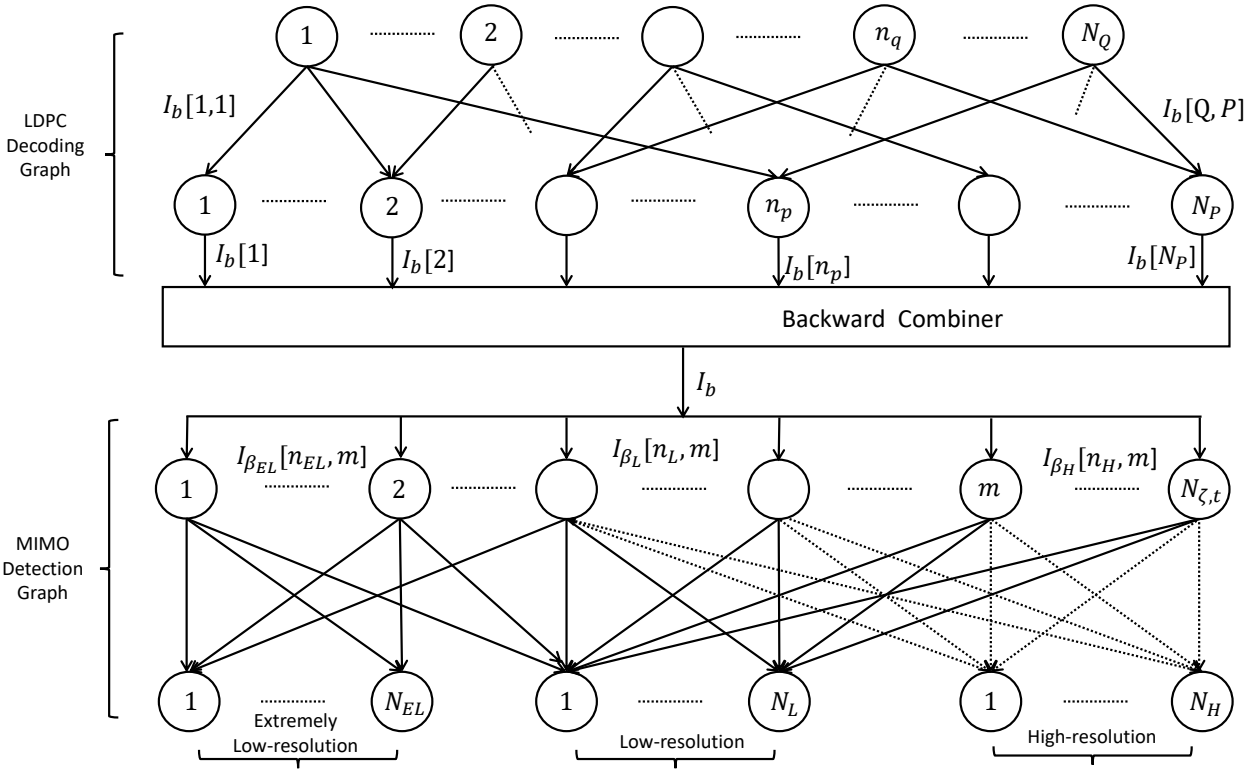

Figure 4. Backward information flow in the proposed triple mixed-ADC LS-MIMO PEXIT framework.

LLR messages from all N_{EL} extremely low-resolution observation nodes, N_{L} LLR messages from all N_{L} low-resolution observation nodes, and N_{H} LLR messages from all N_{H} high-resolution observation nodes. This reflects the broadcast nature of radio transmissions, as depicted by the fully connected graph in Figure 3. For a given realization of the channel matrix $\mathbf{H}_{\tilde{\xi}}$, with $\tilde{\xi} \in \{\mathrm{EL},\mathrm{L},\mathrm{H}\}$, the LLR message transferred from the $n_{\tilde{\xi}}$-th observation node to the m-th variable node, $L_{\gamma_{\tilde{\xi}}}[n_{\tilde{\xi}},m]$, as derived in (24), is given by

$$L_{\gamma,\xi}[n_\xi,m] = \frac{4\varphi_\xi \Re\big(H_\xi^*[n_\xi,m]\,\hat{Y}_\xi[n_\xi,m]\big)}{\Psi_\xi[n_\xi,m]} = \frac{4\Re\Big(\varphi_\xi^2\,|H_\xi[n_\xi,m]|^2\,V_\xi[m] \;+\; \varphi_\xi\,Z_\xi[n_\xi,m]\Big)}{\Psi_\xi[n_\xi,m]} = \frac{4\big(\varphi_\xi^2\,|H_\xi[n_\xi,m]|^2\,V_\xi[m] \;+\; \varphi_\xi\,\Re\big(H_\xi^*[n_\xi,m]\,Z_\xi[n_\xi,m]\big)\big)}{\Psi_\xi[n_\xi,m]}.$$

Without loss of generality, we assume an all-zero codeword is transmitted. Consequently, the LLR value $L_{\gamma,\xi}[n_\xi,m]$ is given by

$$L_{\gamma,\xi}[n_\xi,m] = \frac{4\Big(\varphi_\xi^2\,|H_\xi[n_\xi,m]|^2 \;+\; \varphi_\xi\,\Re\big(H_\xi^*[n_\xi,m]\,Z_\xi[n_\xi,m]\big)\Big)}{\Psi_\xi[n_\xi,m]}.$$

Because $\mathbb{E}\big[Z_\xi[n_\xi,m]\,Z_\xi^*[n_\xi,m]\big] = \Psi_\xi[n_\xi,m]$ (where $\mathbb{E}(\cdot)$ is the expectation operator), we have

$$\big(\varphi_\xi^2\,|H_\xi[n_\xi,m]|^2 \;+\; \varphi_\xi\,\Re\big(H_\xi^*[n_\xi,m]\,Z_\xi[n_\xi,m]\big)\big) \sim \mathcal{N}\Big(\varphi_\xi^2\,|H_\xi[n_\xi,m]|^2,\; \frac{\varphi_\xi^2\,|H_\xi[n_\xi,m]|^2\,\Psi_\xi[n_\xi,m]}{2}\Big). \quad (30)$$

Consequently, we have

$$\gamma_\xi[n_\xi,m] \sim \mathcal{N}\Big(\tfrac{\sigma^2_{\gamma_\xi}[n_\xi,m]}{2},\, \sigma^2_{\gamma_\xi}[n_\xi,m]\Big), \quad (31)$$

where

$$\sigma^2_{\gamma_\xi}[n_\xi,m] = \frac{8\,\varphi_\xi^2\,|H_\xi[n_\xi,m]|^2}{\Psi_\xi[n_\xi,m]}. \quad (32)$$

The LLR $L_{\gamma_\xi}[n_\xi,m]$ follows a symmetric Gaussian distribution for a fixed channel realization [45]. The expression in (31) is derived under the assumption that the interference-plus-noise terms $z_\xi[n_\xi,m]$ are i.i.d. complex Gaussian. In the high-resolution case, both the EXIT chart analysis and simulation results indicate that this assumption remains valid when the number of receive antennas is large [48]. Hence, the mutual information from the n_ξ-th observation node to the m-th symbol node is given by

$$I_{\gamma_\xi}[n_\xi,m] = J\left(\sqrt{\tfrac{8\,\varphi_\xi^2\,|H_\xi[n_\xi,m]|^2}{\Psi_\xi[n_\xi,m]}}\right), \quad \xi \in \{EL,L,H\}, \quad (33)$$

where the function $J(x)$ is defined in [43].

4.1.2 Mutual Information from Symbol Nodes to Variable Nodes: The m-th symbol node collects a total of $N_r = N_{EL} + N_L + N_H$ messages from the N_{EL} extremely low-resolution observation nodes, the N_L low-resolution observation nodes and the N_H high-resolution nodes, as depicted in Figure 3. Defining $L_\gamma[m]$ as the aggregate message at the m-th symbol node, we obtain

$$L_{\gamma,\xi}[m] = \sum_{\xi\in\{EL,L,H\}} \sum_{n_\xi}^{N_\xi} L_{\gamma,\xi}[n_\xi,m]. \quad (34)$$

Following (31), the total message likewise adheres to a Gaussian distribution, with mean and variance given by

$$L_{\gamma,\xi}[m] \sim \mathcal{N}\big(\tfrac{\sigma^2_\gamma[m]}{2},\, \sigma^2_\gamma[m]\big), \quad (35)$$

where

$$\sigma^2_\gamma[m] = \sum_{\xi\in\{EL,L,H\}} \sum_{n_\xi=1}^{N_\xi} \sigma^2_{\gamma_\xi}[n_\xi,m] = \sum_{\xi\in\{EL,L,H\}} \sum_{n_\xi=1}^{N_\xi} \frac{8\,\varphi_\xi^2\,|H_\xi[n_\xi,m]|^2}{\Psi_\xi[n_\xi,m]}, \quad (36)$$

and thus the extrinsic mutual information $I_\gamma[m]$ is obtained by the following equation

$$I_\gamma[m] = J\left(\sqrt{\sum_{\xi\in\{EL,L,H\}} \sum_{n_\xi=1}^{N_\xi} \frac{8\,\varphi_\xi^2\,|H_\xi[n_\xi,m]|^2}{\Psi_\xi[n_\xi,m]}}\right). \quad (37)$$

From (37), we can see how high-resolution ADCs affect the overall mutual information transferred from the observation nodes to the symbol nodes. In particular, high-resolution ADCs provide a larger φ_H and a smaller $\Psi_H[n_H,m]$, which together increase the total variance σ_α^2. As a result, the mutual information conveyed from the observation nodes to the symbol nodes is higher than in conventional low-resolution ADC schemes, where only one ADC resolution is used.

Assuming an infinitely long code length ($N_c \to \infty$), the bits associated with any given variable node are transmitted over all $N_{\xi,t}$ transmit antennas (symbol nodes) with equal probability $1/N_{\xi,t}$. The forward combiner aggregates the mutual information received from all symbol nodes and delivers it to the variable nodes. Let I_γ denote the average mutual information from all symbol nodes. We have

$$I_\gamma = \frac{1}{N_{\xi,t}} \sum_{m=1}^{N_{\xi,t}} I_\gamma[m], \quad (38)$$

where $I_\gamma[m]$ is given in (37).

Hence, the channel mutual information passed from the symbol nodes to the n_p-th variable node is expressed as

$$I_\gamma[n_p] = P_p\,I_\gamma, \quad \forall p = 1,2,\ldots,N_P, \quad (39)$$

where $P_p = 1$ if node n_p is unpunctured, and $P_p = 0$ otherwise.

4.1.3 Mutual Information Flow from Variable Nodes to Check Nodes: The expression for the mutual information transferred from the n_p-th variable node to the n_q-th check node, $I_a[n_p,n_q]$, is identical to that of the conventional PEXIT algorithm in [44] and given by

$$I_a[n_p,n_q] = J\left(\sqrt{[J^{-1}(I_\alpha[n_p])]^2 + \sigma_b^2[n_p]}\right), \quad (40)$$

where

$$\sigma_b^2[n_p] = \sum_{n_t\in\mathcal{N}_c(n_p)\setminus n_p} \mathbf{B}[n_t,n_p]\,[J^{-1}(I_b[n_t,n_p])]^2,$$

where $J^{-1}(x)$ is given in [43].

4.2 Backward Mutual Information Flow

The backward mutual information flow traces the path along which the extrinsic mutual information travels from the check nodes, passing through the variable and symbol nodes, and finally reaching the observation nodes, as illustrated in Figure 4. In what follows, we derive the mutual information functions that propagate in the backward direction.

4.2.1 Mutual Information Flow from Check Nodes to Variable Nodes: The process of determining the mutual information that flows from the q-th check node to the p-th variable node parallels that of the conventional PEXIT algorithm in [44]. We have $I_b[n_q, n_p]$

$$I_b[n_q, n_p] = 1 - J\left(\sigma_a[n_q]\right), \tag{41}$$

where

$$\sigma_a^2[n_q] = \sum_{n_t \in \mathcal{N}_v(n_q)\backslash n_p} \mathbf{B}[n_q, n_t][J^{-1}(1 - I_a[n_t, n_q])]^2.$$

4.2.2 Mutual Information Flow from Variable Nodes to Symbol Nodes: Let $I_b[n_p]$ denote the total mutual information that the n_p-th variable node receives from the check nodes. We can express the total mutual information as below

$$I_b[n_p] = \sum_{n_q \in \mathcal{N}_c(n_p)} I_b[n_q, n_p]. \tag{42}$$

Under the same infinite code length assumption, the probability that any symbol node transmits a codeword bit originating from the n_p-th variable node is $1/\left(\sum_{p=1}^{N_P} P_p\right)$. Consequently, the backward combiner aggregates the mutual information across all variable nodes before forwarding it to the symbol nodes. The average mutual information from the variable nodes to the symbol nodes is thus given by

$$I_b = \frac{\sum_{n_p=1}^{N_P} P_p I_b[n_p]}{\sum_{n_p=1}^{N_P} P_p}. \tag{43}$$

4.2.3 Mutual Information from Symbol Nodes to Observation Nodes: The mutual information conveyed from the m-th symbol node to the n_{EL}-th low-resolution observation node, $I_{\beta_{EL}}[m, n_{EL}]$, is calculated as

$$I_{\beta_{EL}}[m, n_{EL}] = J\left(\sqrt{\sigma^2_{\gamma^*_{EL}}[m] + \sigma^2_{\gamma_L}[m] + \sigma^2_{\gamma_H}[m] + \sigma_b^2}\right), \tag{44}$$

where

$$\sigma_b^2 = [J^{-1}(I_b)]^2,$$

and

$$\begin{aligned}\sigma^2_{\gamma^*_{EL}}[m] &= \sum_{n_t \in \mathcal{N}_{EL,o}(m)\backslash n_{EL}} [J^{-1}(I_{\gamma_{EL}}[n_t, m])]^2 \\ &= \sum_{n_t \in \mathcal{N}_{EL,o}(m)\backslash n_{EL}} \sigma^2_{\gamma_{EL}}[n_t, m] \\ &= \sum_{n_t \in \mathcal{N}_{EL,o}(m)\backslash n_{EL}} \frac{8\varphi^2_{EL}|H_{EL}[n_t, m]|^2}{\Psi_{EL}[n_t, m]}.\end{aligned}$$

The mutual information transferred from the m-th symbol node to the n_L-th low-resolution observation node, $I_{\beta_L}[m, n_L]$, is calculated as

$$I_{\beta_L}[m, n_L] = J\left(\sqrt{\sigma^2_{\gamma^*_L}[m] + \sigma^2_{\gamma_{EL}}[m] + \sigma^2_{\gamma_H}[m] + \sigma_b^2}\right), \tag{45}$$

where

$$\sigma_b^2 = [J^{-1}(I_b)]^2,$$

and

$$\begin{aligned}\sigma^2_{\gamma^*_L}[m] &= \sum_{n_t \in \mathcal{N}_{L,o}(m)\backslash n_L} [J^{-1}(I_{\gamma_L}[n_t, m])]^2 \\ &= \sum_{n_t \in \mathcal{N}_{L,o}(m)\backslash n_L} \sigma^2_{\alpha_L}[n_t, m] \\ &= \sum_{t \in \mathcal{N}_{L,o}(m)\backslash n_L} \frac{8\varphi^2_L|H_L[n_t, m]|^2}{\Psi_L[n_t, m]}.\end{aligned}$$

The mutual information transferred from the m-th symbol node to the n_H-th high-resolution observation node, $I_{\beta_H}[m, n_H]$, is calculated as

$$I_{\beta_H}[m, n_H] = J\left(\sqrt{\sigma^2_{\gamma^*_H}[m] + \sigma^2_{\gamma_{EL}}[m] + \sigma^2_{\gamma_L}[m] + \sigma_b^2}\right), \tag{46}$$

where

$$\begin{aligned}\sigma^2_{\gamma^*_H}[m] &= \sum_{n_t \in \mathcal{N}_{H,o}(m)\backslash n_H} [J^{-1}(I_{\gamma_H}[n_t, m])]^2 \\ &= \sum_{n_t \in \mathcal{N}_{H,o}(m)\backslash n_H} \sigma^2_{\gamma_H}[n_t, m] \\ &= \sum_{n_t \in \mathcal{N}_{H,o}(m)\backslash n_H} \frac{8\varphi^2_H|H_H[n_t, m]|^2}{\Psi_H[n_t, m]}.\end{aligned}$$

The expressions in (44), (45), and (46) illustrate the interaction among extremely low-resolution, low-resolution, and high-resolution ADCs. Due to the fully connected graph structure, mutual information from the high-resolution nodes propagates to the low-resolution observation nodes via the symbol nodes, thereby increasing the mutual information of the low-resolution nodes, and *vice versa*. This exchange plays an important role in enhancing the performance of mixed-ADC LS-MIMO systems, as will be further examined in the following sections.

4.3 The APP mutual information

Calculate $I_\Gamma[n_p]$ for the n_p-th variable node

$$I_\Gamma[n_p] = J\left(\sqrt{[J^{-1}(I_\alpha[n_p])]^2 + \sigma_b^2[n_p]}\right), \tag{47}$$

where

$$\sigma_b^2[n_p] = \sum_{n_t \in \mathcal{N}_c(n_p)} \mathbf{B}[n_t, n_p][J^{-1}(I_b[n_t, n_p])]^2.$$

4.4 Proposed PEXIT Algorithm For LS-MIMO Communication Systems With Triple-Mixed ADCs

The proposed PEXIT procedure is obtained by combining the mutual-information functions derived in the

preceding subsections with the parameters of a given LS-MIMO configuration ($N_t \times N_r$), the proto-matrix $\mathbf{B}$ of size $N_Q \times N_P$, the channel parameter E_b/N_0, and the resolution levels of the triple mixed-ADCs Q_{EL}, Q_{L}, and Q_{H}. The resulting mixed-ADC LS-MIMO-PEXIT algorithm is summarised as follows:

Step 0: Initialization:

- Select the size of proto-matrix: $\mathbf{B}$
- Calculate the coding rate: $R_c = \frac{N_P - N_Q}{\sum_{np=1}^{N_P} P_p}$
- Calculate $N_0 = \frac{N_t}{R(E_b/N_0)}$
- Obtain the values of φ_{EL}, φ_L and φ_H from Table I accordingly their resolution levels Q_{EL}, Q_L and Q_H, respectively
- Set $I_{\beta_{EL}} = 0$, $I_{\beta_L} = 0$ and $I_{\beta_H} = 0$
- Generate $3 \times F$ LS-MIMO channel realization matrices $\{\mathbf{H}_{\xi,1}, \mathbf{H}_{\xi,2}, \cdots, \mathbf{H}_{\xi,F}\}, \xi \in \{EL, L, H\}$ which follow Rayleigh distribution
- Set the parameters for the superposition modulation to M, calculate $G = \log_2(M)/2$
- Set values to $\alpha_{I,1}, \alpha_{I,2}, \cdots, \alpha_{I,G}$
- Set values to $\alpha_{Q,1}, \alpha_{Q,2}, \cdots, \alpha_{Q,G}$

Step 1: Preprocessing

- Forming matrices $\boldsymbol{\alpha}_I$ and $\boldsymbol{\alpha}_Q$
- For each $f = 1, 2, \cdots, F$, calculate $H_{\xi,f}$

Step 2: Observation to variable update

- For $f = 1, 2, \cdots, F$
  - For $m = 1, 2, \cdots, N_{\xi,t}$ and $n_\xi = 1, 2, \cdots, N_\xi, \xi \in \{EL, L, H\}$
    - Calculate $\sigma_{\beta_\xi} = J^{-1}(I_{\beta_\xi})$
    - Generate $\beta_{\xi,f}[m, n_\xi] \sim \mathcal{N}\left(\pm\frac{\sigma^2_{\beta_\xi}}{2}, \sigma^2_{\beta_\xi}\right)$
    - Estimate soft information $\hat{V}_f[m, n_\xi] = \tanh\left(\frac{\beta_{\xi,f}[m,n_\xi]}{2}\right)$
    - Calculate $\Psi_{\xi,f}[n_\xi, m]$ by using formula (23).
  - For $m = 1, 2, \cdots, N_t$
    - Calculate $I_{\gamma,f}[m]$ by using formula (37)
- Calculate the average of $I_{\gamma,f}$ over all the channel realizations

$$I_\gamma[m] = \frac{1}{F}\sum_{f=1}^{F} I_{\gamma,f}[m], \forall m = 1, 2, \cdots, N_{\xi,t}.$$

- For $n_p = 1, 2, \cdots, N_P$, calculate $I_\gamma[n_p]$

$$I_\alpha[n_p] = P_p\left(\frac{1}{N_{\xi,t}}\sum_{m=1}^{N_{\xi,t}} I_\gamma[m]\right).$$

Note that if the n_p-th variable node is punctured, then $P_p = 0$. Otherwise, $P_p = 1$.

Step 3: Variable to check update

- For $n_p = 1, 2, \cdots, N_P$ and $n_q = 1, 2, \cdots, N_Q$, calculate $I_a[n_p, n_q]$:
  - if $\mathbf{B}[n_p, n_q] \neq 0$, $I_a[n_p, n_q]$ is then calculated by using formula (40)
  - If $\mathbf{B}[n_p, n_q] = 0$, $I_a[n_p, n_q] = 0$.

Step 4: Check to variable update

- For $n_q = 1, 2, \cdots, N_Q$ and $n_p = 1, 2, \cdots, N_P$
  - if $\mathbf{B}[n_q, n_p] \neq 0$, $I_b[n_q, n_p]$ is then calculated by using formula (41)
  - If $\mathbf{B}[n_q, n_p] = 0$, $I_b[n_q, n_p] = 0$

Step 5: Symbol to observation update

- For $f = 1, 2, \cdots, F$
  - For $m = 1, 2, \cdots, N_{\xi,t}$ and $n_{EL} = 1, 2, \cdots, N_{EL}$, $I_{\beta_{EL},f}[m, n_{EL}]$ is then calculated by using (44)
  - For $m = 1, 2, \cdots, N_{\xi,t}$ and $n_L = 1, 2, \cdots, N_L$, $I_{\beta_L,f}[m, n_L]$ is then calculated by using (45)
  - For $m = 1, 2, \cdots, N_{\xi,t}$ and $n_H = 1, 2, \cdots, N_H$, $I_{\beta_{H,f}}[m, n_H]$ is calculated by using formula (46)
- For $m = 1, 2, \cdots, N_{\xi,t}$ and $n_{EL} = 1, 2, \cdots, N_{EL}$

$$I_{\beta_L}[m, n_{EL}] = \frac{1}{F}\sum_{f=1}^{F} I_{\beta_{EL,f}}[m, n_{EL}]$$

- For $m = 1, 2, \cdots, N_{\xi,t}$ and $n_L = 1, 2, \cdots, N_L$

$$I_{\beta_L}[m, n_L] = \frac{1}{F}\sum_{f=1}^{F} I_{\beta_{L,f}}[m, n_L]$$

- For $m = 1, 2, \cdots, N_{\xi,t}$ and $n_H = 1, 2, \cdots, N_H$

$$I_{\beta_H}[m, n_H] = \frac{1}{F}\sum_{f=1}^{F} I_{\beta_{H,f}}[m, n_H]$$

Step 6: APP-LLR mutual information calculation

- For $n_p = 1, 2, \cdots, N_P$, $I_\Gamma[n_p]$ is then calculated by using formula (47)

Step 7: Repeat Step 1 - Step 6 until $I_\Gamma[n_p] = 1$, $\forall n_p = 1, 2, \cdots, N_P$.

The modified PEXIT algorithm is considered to have converged when the selected E_b/N_0 exceeds the threshold. The threshold $(E_b/N_0)^*$ is defined as the minimum E_b/N_0 at which the mutual information between the APP-LLR messages and the corresponding codeword bits converges to 1.

Compared with the uniform low-resolution ADC version [12] and the dual mixed-ADC version [49], the triple mixed-ADC PEXIT algorithm differs in all steps except Step 3. In particular, the mutual interaction among the extremely low-resolution, low-resolution, and high-resolution ADCs is explicitly incorporated when computing the mutual information along the double-layer graph. In the next section, this PEXIT algorithm is applied to evaluate the performance of LS-MIMO systems with mixed-ADCs under two previously designed protograph LDPC codes. The resulting iterative decoding thresholds are used to assess the potential advantages of the triple mixed-ADC approach.

5 Theoretical Performance Analysis

In this section, the proposed mixed-ADC LS-MIMO PEXIT algorithm from the previous section is used to calculate the iterative decoding thresholds of two specific protograph LDPC codes: the code in (48), designed for LS-MIMO channels [28], and the code in (49), constructed for AWGN channels [50]. The corresponding proto-matrices are given in (48) and (49). The PEXIT

algorithm is employed to theoretically compare the performance of the equal-distance and equal-weight SM schemes. In addition, the analysis examines the performance gains achieved with mixed-ADC architectures relative to single-ADC systems.

$$\mathbf{B}_{3\times 6} = \begin{bmatrix} 3 & 1 & 0 & 1 & 0 & 1 \\ 2 & 1 & 2 & 2 & 1 & 0 \\ 3 & 2 & 1 & 0 & 1 & 0 \end{bmatrix}, \tag{48}$$

$$\mathbf{B}_{4\times 8} = \begin{bmatrix} 3 & 3 & 0 & 0 & 1 & 0 & 0 & 0 \\ 2 & 3 & 0 & 1 & 0 & 1 & 0 & 0 \\ 3 & 2 & 1 & 0 & 0 & 2 & 1 & 1 \\ 0 & 0 & 2 & 2 & 2 & 0 & 2 & 1 \end{bmatrix}. \tag{49}$$

In this experiment, we evaluate a 10×40 LS-MIMO system with a 3×6 code structure under four resolution modes: single 1-bit ADCs, dual mixed-ADCs ($N_{\mathrm{L}} = 35$, $N_{\mathrm{H}} = 5$), triple mixed-ADCs ($N_{\mathrm{EL}} = 25$, $N_{\mathrm{L}} = 10$, $N_{\mathrm{H}} = 5$), and single 5-bit ADCs. Table II compares their decoding thresholds for both equal-distance and equal-weight SM schemes.

Across all resolution modes, the equal-weight SM consistently achieves lower thresholds than the equal-distance SM, with an advantage of roughly 1 dB. This gap narrows slightly as ADC resolution increases, decreasing from 1.19 dB in the single 1-bit ADC case to 0.97 dB in the single 5-bit ADC case. Transitioning from a single 1-bit ADC configuration to a triple mixed-ADC architecture yields notable improvements, lowering the required decoding threshold by approximately 1.14 dB for the equal-distance SM and 1.03 dB for the equal-weight SM. Nevertheless, the triple mixed-ADC setup still exhibits a gap of about 1.7 dB compared to the single 5-bit ADC performance, albeit with a much lower number of high-resolution components. This observation raises the question of the optimal trade-off between power consumption and performance. It is worth noting that ADC power consumption grows exponentially with resolution. Therefore, replacing most high-resolution converters with 1–2 bit ADCs yields substantial power savings. At the same time, our results show that retaining even a small fraction of 5-bit ADCs allows iterative decoding thresholds close to the 5-bit baseline, striking a favorable balance between performance and energy cost.

Table II
Decoding thresholds (in dB) for a 6×3 protograph LDPC code in a 10×40 LS-MIMO system under different ADC configurations: single 1-bit ADCs, dual mixed-ADCs ($N_{\mathrm{L}} = 35$, $N_{\mathrm{H}} = 5$), triple mixed-ADCs ($N_{\mathrm{EL}} = 25$, $N_{\mathrm{L}} = 10$, $N_{\mathrm{H}} = 5$), and single 5-bit ADCs. Equal-distance (ED) and equal-weight (EW) SM schemes are compared, with the gap representing the difference ED−EW

Resolution Mode	ED (dB)	EW (dB)	Gap (dB)
Single 1-bit ADCs	1.34	0.15	1.19
Dual mixed-ADCs	0.77	-0.34	1.11
Triple mixed-ADCs	0.19	-0.88	1.07
Single 5-bit ADCs	-1.57	-2.54	0.97

In the experiment summarised in Table III, we evaluate a 10×60 LS-MIMO system with a 3×6 code structure under four resolution modes: single 1-bit ADCs, dual mixed-ADCs ($N_{\mathrm{L}} = 40$, $N_{\mathrm{H}} = 20$), triple mixed-ADCs ($N_{\mathrm{EL}} = 40$, $N_{\mathrm{L}} = 10$, $N_{\mathrm{H}} = 10$), and single 5-bit ADCs. As in the 10×40 configuration, the results show that equal-weight SM scheme consistently achieves lower thresholds than equal-distance SM, with the gap for each resolution mode remaining close to 1 dB.

Both dual and triple mixed-ADC architectures again outperform the single 1-bit ADC baseline, reflecting similar gains to those observed in the previous experiment. For example, in the equal-distance SM scheme, the triple mixed-ADC configuration achieves an iterative decoding threshold of -1.72 dB, compared with -0.79 dB for the single 1-bit ADC case.

Table III
Decoding thresholds (in dB) for a 3×6 protograph LDPC code in a 10×60 LS-MIMO system under different ADC configurations: single 1-bit ADCs, dual mixed-ADCs ($N_{\mathrm{L}} = 40$, $N_{\mathrm{H}} = 20$), triple mixed-ADCs ($N_{\mathrm{EL}} = 40$, $N_{\mathrm{L}} = 10$, $N_{\mathrm{H}} = 10$), and single 5-bit ADCs. Equal-distance (ED) and equal-weight (EW) SM schemes are compared, with the gap representing ED−EW

Resolution Mode	ED (dB)	EW (dB)	Gap (dB)
Single 1-bit ADCs	−0.79	−1.91	1.12
Dual mixed-ADCs	−1.39	−2.46	1.07
Triple mixed-ADCs	−1.72	−2.77	1.05
Single 5-bit ADCs	−3.35	−4.34	0.99

In another experiment, summarised in Table IV, we evaluate a 10×80 LS-MIMO system with a 3×6 code structure under four resolution modes: single 1-bit ADCs, dual mixed-ADCs ($N_{\mathrm{L}} = 60$, $N_{\mathrm{H}} = 20$), triple mixed-ADCs ($N_{\mathrm{EL}} = 60$, $N_{\mathrm{L}} = 10$, $N_{\mathrm{H}} = 10$), and single 5-bit ADCs. Consistent with the results for the 10×40 and 10×60 configurations, equal-weight SM scheme achieves lower thresholds than equal-distance one across all ADC settings, with an advantage of approximately 1 dB.

Moving from a single 1-bit ADC (-2.22 dB) to either the dual or triple mixed-ADC configurations (-2.63 dB and -2.87 dB, respectively, for the equal-distance SM) yields notable threshold improvements, following the same pattern observed in earlier experiments. In particular, the triple mixed-ADC scheme achieves an additional 0.24 dB gain over the dual mixed-ADC setup, highlighting the incremental benefit of incorporating a third resolution tier.

Table IV
Decoding thresholds (in dB) for a 3×6 protograph LDPC code in a 10×80 LS-MIMO system under different ADC configurations: single 1-bit ADCs, dual mixed-ADCs ($N_{\mathrm{L}} = 60$, $N_{\mathrm{H}} = 20$), triple mixed-ADCs ($N_{\mathrm{EL}} = 60$, $N_{\mathrm{L}} = 10$, $N_{\mathrm{H}} = 10$), and single 5-bit ADCs. Equal-distance (ED) and equal-weight (EW) SM schemes are compared, with the gap representing ED−EW

Resolution Mode	ED (dB)	EW (dB)	Gap (dB)
Single 1-bit ADCs	−2.22	−3.30	1.08
Dual mixed-ADCs	−2.63	−3.69	1.06
Triple mixed-ADCs	−2.87	−3.92	1.05
Single 5-bit ADCs	−4.62	−5.61	0.99

In the experiment summarised in Table V, we evaluate the iterative decoding thresholds of the 4×8 protograph code—originally designed for an AWGN channel—under the same 10×40 LS-MIMO configuration used earlier for the 3×6 LDPC code. The results in Table V show trends consistent with those in Table II: equal-weight SM achieves lower thresholds than its equal-distance counterpart, and mixed-ADC architectures (both dual and triple) provide substantial gains over the single 1-bit ADC baseline.

However, a clear difference is observed in the absolute threshold values. Across all resolution modes, the 4×8 AWGN code exhibits higher thresholds compared with the 3×6 LDPC code. For example, in the equal-distance SM scheme, the single 1-bit ADC threshold increases from 1.34 dB to 1.68 dB, while the triple mixed-ADC threshold rises by 0.26 dB (from 0.15 dB to 0.41 dB). These results suggest that although both codes follow similar performance trends when moving from low- to higher-resolution ADCs, the LS-MIMO-optimised code consistently achieves lower thresholds in the same LS-MIMO configuration, highlighting the benefits of channel-specific LDPC code design.

Table V
Decoding thresholds (in dB) for an 4×8 protograph LDPC code (designed for AWGN channels) in a 10×40 LS-MIMO system under different ADC configurations: single 1-bit ADCs, dual mixed-ADCs ($N_{\mathrm{L}} = 35$, $N_{\mathrm{H}} = 5$), triple mixed-ADCs ($N_{\mathrm{EL}} = 25$, $N_{\mathrm{L}} = 10$, $N_{\mathrm{H}} = 5$), and single 5-bit ADCs. Equal-distance (ED) and equal-weight (EW) SM schemes are compared, with the gap representing ED−EW

Resolution Mode	ED (dB)	EW (dB)	Gap (dB)
Single 1-bit ADCs	1.68	0.41	1.27
Dual mixed-ADCs	1.09	−0.09	1.18
Triple mixed-ADCs	0.49	−0.64	1.13
Single 5-bit ADCs	−1.29	−2.33	1.04

The performance of an 4×8 protograph code—designed for an AWGN channel—under the 10×60 MIMO configuration is evaluated, with the resulting iterative decoding thresholds shown in Table VI. While the results follow similar trends to those observed for the 3×6 LDPC code—namely, improvements when moving from single 1-bit ADCs to dual and triple mixed-ADC configurations, and from equal-distance to equal-weight SM—the absolute threshold values differ noticeably. For example, in the single 1-bit ADC setting, the equal-distance threshold of -0.47 dB for the AWGN-oriented code is higher than the -0.79 dB obtained with the LS-MIMO-optimised code in Table III, representing a 0.32 dB difference under identical conditions. This higher threshold is observed across all resolution modes, even though each mixed-ADC configuration still outperforms its single 1-bit counterpart. Overall, while the performance trends remain consistent—reinforcing the benefits of mixed-ADC architectures and equal-weight SM—the LS-MIMO-specific code consistently achieves lower thresholds in the same LS-MIMO configuration, highlighting the importance of tailoring LDPC code designs to the target channel environment.

Table VI
Decoding thresholds (in dB) for an 4×8 protograph LDPC code (AWGN-optimised) in a 10×60 LS-MIMO system under different ADC configurations: single 1-bit ADCs, dual mixed-ADCs ($N_{\mathrm{L}} = 40$, $N_{\mathrm{H}} = 20$), triple mixed-ADCs ($N_{\mathrm{EL}} = 40$, $N_{\mathrm{L}} = 10$, $N_{\mathrm{H}} = 10$), and single 5-bit ADCs. Equal-distance (ED) and equal-weight (EW) SM schemes are compared, with the gap representing ED−EW

Resolution Mode	ED (dB)	EW (dB)	Gap (dB)
Single 1-bit ADCs	−0.47	−1.66	1.19
Dual mixed-ADCs	−1.09	−2.22	1.13
Triple mixed-ADCs	−1.43	−2.54	1.11
Single 5-bit ADCs	−3.08	−4.12	1.04

Finally, we evaluate the 4×8 code under the same 10×80 LS-MIMO configuration considered for the 3×6 code in Table IV. The results follow the same general trend observed previously: thresholds decrease progressively as ADC resolution increases, and the performance gap between equal-weight and equal-distance SM remains in the range of 1.04 dB to 1.15 dB. The gain from adopting a triple mixed-ADC configuration, relative to the single 1-bit ADC baseline, decreases from 0.96 dB in the 10×60 LS-MIMO case to 0.67 dB in the 10×80 setup.

Table VII
Decoding thresholds (in dB) for an 4×8 protograph LDPC code (AWGN-optimised) in a 10×80 LS-MIMO system under different ADC configurations: single 1-bit ADCs, dual mixed-ADCs ($N_{\mathrm{L}} = 60$, $N_{\mathrm{H}} = 20$), triple mixed-ADCs ($N_{\mathrm{EL}} = 60$, $N_{\mathrm{L}} = 10$, $N_{\mathrm{H}} = 10$), and single 5-bit ADCs. Equal-distance (ED) and equal-weight (EW) SM schemes are compared, with the gap representing ED−EW

Resolution Mode	ED (dB)	EW (dB)	Gap (dB)
Single 1-bit ADCs	−1.91	−3.06	1.15
Dual mixed-ADCs	−2.33	−3.45	1.12
Triple mixed-ADCs	−2.58	−3.69	1.11
Single 5-bit ADCs	−4.35	−5.39	1.04

6 Simulation Results

In this section, computer simulations are conducted to validate the theoretical decoding thresholds reported in the previous section. The simulation setup follows that of the theoretical analysis, considering three MIMO configurations—10×40, 10×60, and 10×80—and two previously designed protograph LDPC codes with proto-matrices given in (48) and (49).

The LDPC code length of 2400 bits is obtained through two copy-and-permutation (lifting) steps. In the first step, the base protograph is lifted by a factor of 4 using the Progressive Edge Growth (PEG) algorithm [51] to eliminate multiple parallel edges. In the second step, the lifting factor is chosen according to the target information block length. In this work, the protograph contains three check nodes and six variable nodes; applying a lifting factor of 100 yields an information block length of 1200 bits and a total

code length of 2400 bits at the encoder output. During this second lifting stage, the PEG algorithm is again used to select a circulant permutation for each edge class, thereby avoiding short cycles in the resulting LDPC code.

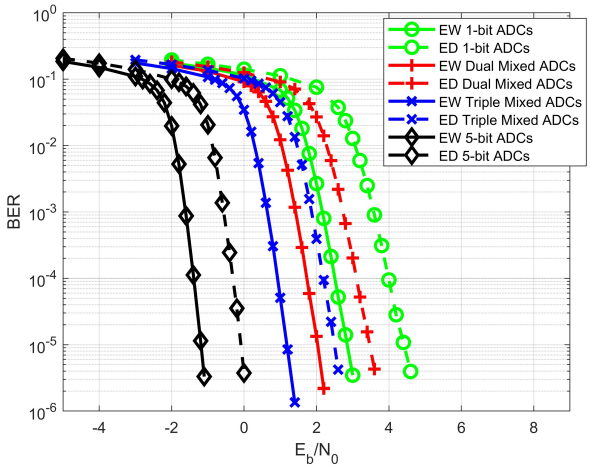

Figure 5. BER performance of the 3×6 protograph LDPC code in (48) with a code length of 2400 bits in a 10×40 LS-MIMO system using a 16-ary constellation and ADC resolutions ranging from 1 to 5 bits.

To begin with, Figure 5 shows the BER performance of different ADC configurations under both equal-weight (EW) and equal-distance (ED) superposition modulation, using the protograph LDPC code defined by the 3×6 proto-matrix. The results correspond to a 10×40 LS-MIMO system with 16-ary superposition modulation. The simulation curves closely match the theoretical predictions in Table II. In all ADC configurations, EW superposition modulation outperforms ED, with gains ranging from approximately 1.0 to 1.8 dB at a BER of 10^{-5}. These gains are consistent with the decoding threshold differences reported in Table II, where EW modulation achieved lower thresholds across all configurations.

In terms of ADC architecture, the triple mixed-ADC configuration—comprising 25 one-bit, 10 two-bit, and 5 five-bit ADCs—achieves a 1.8 dB BER improvement over the single 1-bit system. The dual mixed-ADC configuration also yields a notable gain compared to the single 1-bit case, though its performance remains slightly below that of the triple mixed-ADC setup. These results confirm that the proposed mixed-ADC receiver offers a strong balance between performance and energy efficiency, consistent with the PEXIT-based theoretical predictions. Specifically, the triple mixed-ADC system with EW modulation operates within 1.8 dB of the 5-bit baseline, whereas the 1-bit system lags by more than 3 dB, demonstrating the effectiveness of heterogeneous ADC deployment in LS-MIMO systems. Furthermore, the performance gap between equal-weight and equal-distance superposition modulation decreases as ADC resolution increases. This trend, evident in both the theoretical decoding thresholds (Table II) and the BER curves (Figure 5), suggests that higher-resolution ADCs diminish the relative advantage of optimal SM weighting due to improved quantization precision.

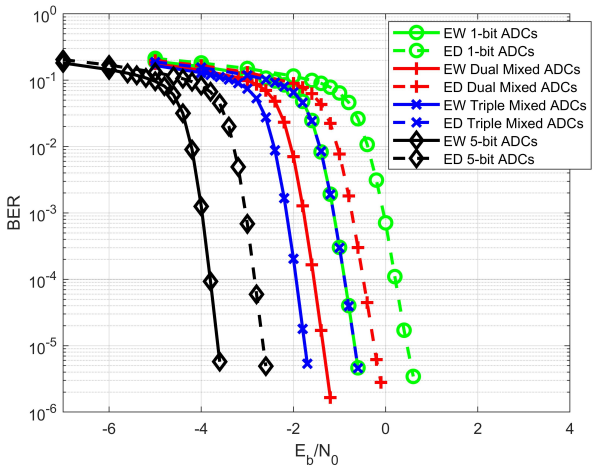

Figure 6. BER performance of the 3×6 protograph LDPC code in (48) with a code length of 2400 bits in a 10×60 LS-MIMO system using a 16-ary constellation and ADC resolutions from 1 to 5 bits.

Figure 6 illustrates the BER performance of the protograph LDPC code defined by the 3×6 proto-matrix in a 10×60 LS-MIMO system with 16-ary superposition modulation. As in the 10×40 configuration (Figure 5), equal-weight (EW) superposition modulation consistently outperforms its equal-distance (ED) counterpart across all ADC configurations, including single 1-bit, dual mixed, triple mixed, and full-resolution 5-bit ADCs, confirming the robustness of EW modulation in diverse quantization environments.

Increasing the number of receive antennas from $N_r = 40$ to $N_r = 60$ yields a significant BER improvement for all configurations. The decoding curves for all ADC architectures shift left by approximately 2–4 dB, indicating that the added spatial diversity enhances detection capability and mitigates quantization noise. This effect is particularly pronounced in low-resolution settings: for example, the 1-bit ADC system with ED modulation now achieves a BER of 10^{-5} at 0.4 dB in the 10×60 LS-MIMO configuration, compared to 4 dB in the 10×40 case.

Furthermore, Figure 7 shows the BER performance of various quantization schemes in a 10×80 LS-MIMO system using the 3×6 protograph LDPC code and a 16-ary SM scheme. The simulation results closely match the theoretical decoding thresholds presented earlier, particularly for the triple mixed-ADC configuration, confirming the accuracy and practical relevance of the proposed mutual-information-based PEXIT analysis framework for systems with heterogeneous quantization.

Increasing the number of receive antennas from $N_r = 40$ to $N_r = 80$ further enhances receive diversity, enabling reliable communication at significantly lower E_b/N_0 values. This benefit is evident from the leftward shift of all BER curves. Nonetheless, the performance gap between the single 1-bit ADC system and the mixed-ADC architectures remains large. For instance, the triple mixed-ADC

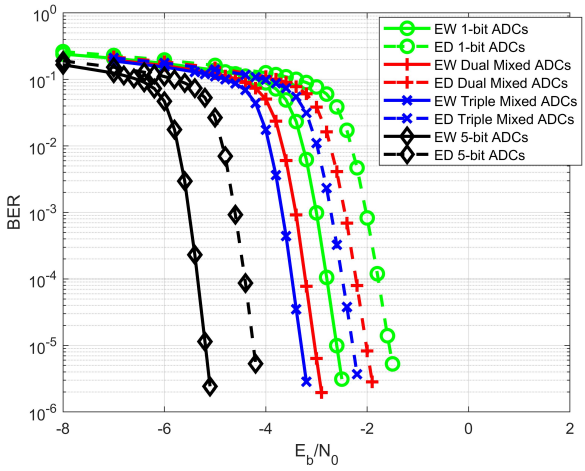

Figure 7. BER performance of the 3×6 protograph LDPC code in (48) with a code length of 2400 bits in a 10×80 LS-MIMO system using a 16-ary constellation and ADC resolutions from 1 to 5 bits.

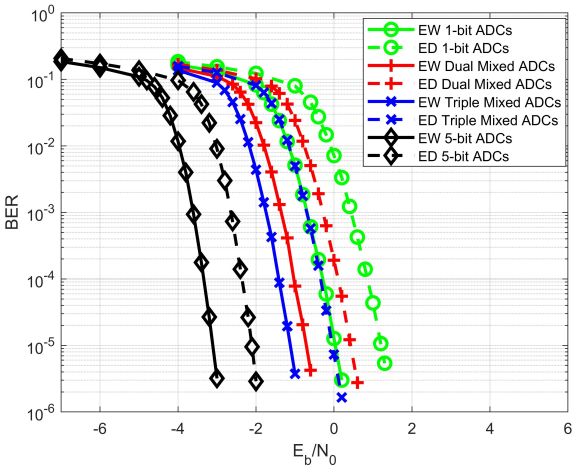

Figure 9. BER performance of the 4×8 protograph LDPC code in (49) with a code length of 2400 bits in a 10×60 LS-MIMO system using a 16-ary constellation and ADC resolutions from 1 to 5 bits.

design with equal-weight modulation achieves a gain of more than 2.2 dB at a BER of 10^{-5} compared with the single 1-bit case.

The performance gap between equal-weight and equal-distance SM narrows slightly for the 1-bit ADC system, decreasing from 1.27 dB in the 10×40 setup to 1.15 dB in the 10×80 case. This reduction is attributed to increased receiver diversity, which lessens the relative impact of symbol weighting. In contrast, for both dual and triple mixed-ADC systems, the equal-weight advantage remains approximately 1 dB, independent of the number of receive antennas.

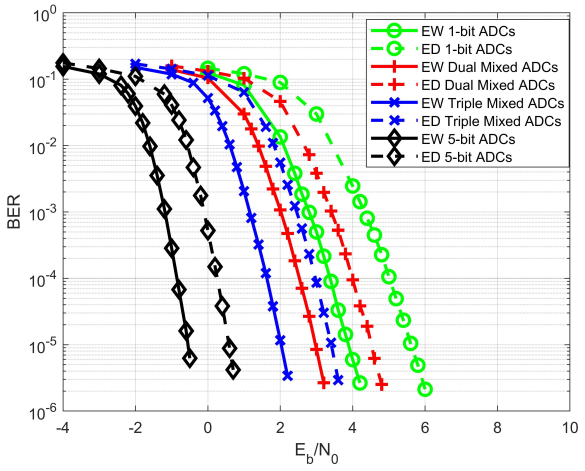

Figure 8. BER performance of the 4×8 protograph LDPC code in (49) with a code length of 2400 bits in a 10×40 LS-MIMO system using a 16-ary constellation and ADC resolutions from 1 to 5 bits.

To compare the performance of the LS-MIMO and AWGN-oriented codes, Figs. 8–10 show the BER curves for the 4×8 protograph LDPC code, originally designed for AWGN channels [50], under various LS-MIMO configurations and ADC resolutions. Although structurally different from the 3×6 protograph used in Figures 5–7, the overall performance trends are similar. In particular, equal-weight (EW) SM consistently

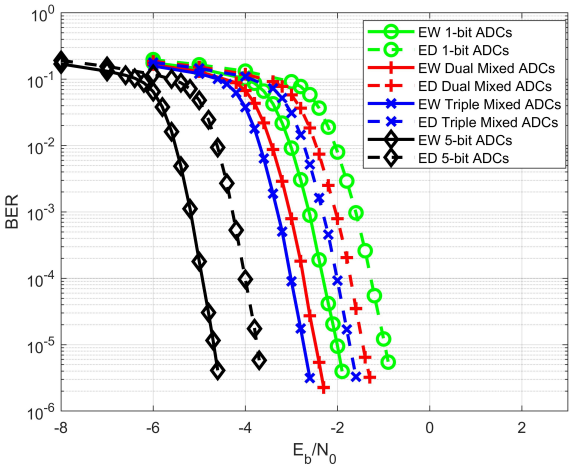

Figure 10. BER performance of the 4×8 protograph LDPC code in (49) with a code length of 2400 bits in a 10×80 LS-MIMO system using a 16-ary constellation and ADC resolutions from 1 to 5 bits.

outperforms equal-distance (ED) modulation across all receiver configurations, and mixed-ADC architectures achieve substantial gains over the single 1-bit ADC baseline. Furthermore, increasing the number of receive antennas from $N_r = 40$ to $N_r = 80$ reduces the required E_b/N_0 to achieve a given BER, demonstrating the benefits of spatial diversity.

The simulation results also agree well with the theoretical thresholds predicted by the proposed mixed-ADC PEXIT analysis, confirming the robustness and applicability of the framework across different code structures. Notably, despite the 4×8 code having more variable and check nodes—often associated with stronger performance in AWGN channels—it underperforms compared with the 3×6 code specifically designed for low-resolution ADCs in massive LS-MIMO channels. For example, under identical system parameters, the 3×6 code consistently achieves lower BER at the same E_b/N_0 levels. These results highlight the importance of tailoring LDPC code design to the characteristics of quantized LS-MIMO channels (e.g., mixed-

ADC distortion and spatial correlation), suggesting a promising avenue for future research.

7 Conclusion

This paper has addressed the energy bottleneck in LS-MIMO receivers by proposing a receiver architecture that integrates triple mixed-resolution ADCs, SM scheme, and protograph LDPC coding. A key contribution is the derivation of a receiver algorithm based on a double-layer factor-graph detector and a tailored LDPC decoder for scenarios employing three different ADC resolutions, along with a triple mixed-ADC PEXIT algorithm capable of accurately predicting iterative decoding thresholds under quantized conditions. The proposed framework enables performance evaluation across different SM schemes and MIMO configurations.

The results presented here provide a foundation for further studies, such as investigating partitioning strategies for the three resolution levels in triple mixed-ADC architectures to balance performance and complexity. Additionally, extending the framework to cooperative transmission scenarios—where SM is particularly well-suited—represents a promising direction for future research.

An important extension is to incorporate robust channel estimation into the triple mixed-ADC framework. Promising directions include leveraging high-resolution branches to assist low-resolution channel estimation, applying quantization-aware linear estimators (e.g., Bussgang-based), and exploiting deep-learning-based pilot processing. These methods may reduce the performance gap under imperfect CSI.

Although we tested 10×40, 10×60, and 10×80 systems in this paper, the proposed analysis and receiver framework are scalable to very large antenna arrays (e.g., 64×64 or beyond), which are expected in 6G deployments. Preliminary results for a 64×64 configuration confirm this scalability and will be reported in future work.

References

[1] D. C. Araújo, T. Maksymyuk, A. L. F. de Almeida, T. Maciel, J. C. M. Mota, and M. Jo, "Massive MIMO: survey and future research topics," *IET Communications*, vol. 10, no. 15, pp. 1938–1946, 2016.

[2] K. B. Letaief, W. Chen, Y. Shi, J. Zhang, and Y. A. Zhang, "The Roadmap to 6G: AI Empowered Wireless Networks," *IEEE Communications Magazine*, vol. 57, no. 8, pp. 84–90, Aug. 2019.

[3] Z. Zhang, Y. Xiao, Z. Ma, M. Xiao, Z. Ding, X. Lei, G. K. Karagiannidis, and P. Fan, "6G Wireless Networks: Vision, Requirements, Architecture, and Key Technologies," *IEEE Vehicular Technology Magazine*, vol. 14, no. 3, pp. 28–41, Sep. 2019.

[4] L. Fan, S. Jin, C. Wen, and H. Zhang, "Uplink Achievable Rate for Massive MIMO Systems With Low-Resolution ADC," *IEEE Communications Letters*, vol. 19, no. 12, pp. 2186–2189, Dec 2015.

[5] J. Zhang, L. Dai, X. Li, Y. Liu, and L. Hanzo, "On Low-Resolution ADCs in Practical 5G Millimeter-Wave Massive MIMO Systems," *IEEE Communications Magazine*, vol. 56, no. 7, pp. 205–211, 2018.

[6] C. Zhang, Y. Jing, Y. Huang, and X. You, "Massive MIMO with Ternary ADCs," *IEEE Signal Processing Letters*, p. 1, 2020.

[7] T. Liu, J. Tong, Q. Guo, J. Xi, Y. Yu, and Z. Xiao, "Energy Efficiency of Massive MIMO Systems With Low-Resolution ADCs and Successive Interference Cancellation," *IEEE Transactions on Wireless Communications*, vol. 18, no. 8, pp. 3987–4002, Aug. 2019.

[8] J. Dai, J. Liu, J. Wang, J. Zhao, C. Cheng, and J. Wang, "Achievable Rates for Full-Duplex Massive MIMO Systems With Low-Resolution ADCs/DACs," *IEEE Access*, vol. 7, pp. 24 343–24 353, 2019.

[9] S. Gao, P. Dong, Z. Pan, and G. Y. Li, "Deep Learning Based Channel Estimation for Massive MIMO With Mixed-Resolution ADCs," *IEEE Communications Letters*, vol. 23, no. 11, pp. 1989–1993, Nov. 2019.

[10] L. V. Nguyen, D. T. Ngo, N. H. Tran, A. L. Swindlehurst, and D. H. N. Nguyen, "Supervised and Semi-Supervised Learning for MIMO Blind Detection with Low-Resolution ADCs," *IEEE Transactions on Wireless Communications*, p. 1, 2020.

[11] L. Xu, X. Lu, S. Jin, F. Gao, and Y. Zhu, "On the Uplink Achievable Rate of Massive MIMO System with Low-Resolution ADC and RF Impairments," *IEEE Communications Letters*, vol. 23, no. 3, pp. 502–505, Mar. 2019.

[12] T. V. Nguyen, H. D. Vu, D. N. Nguyen, and H. T. Nguyen, "Performance Analysis of Protograph LDPC Codes Over Large-Scale MIMO Channels With Low-Resolution ADCs," *IEEE Access*, vol. 7, pp. 145 145–145 160, 2019.

[13] Y. Cho and S. Hong, "One-Bit Successive-Cancellation Soft-Output (OSS) Detector for Uplink MU-MIMO Systems With One-Bit ADCs," *IEEE Access*, vol. 7, pp. 27 172–27 182, 2019.

[14] F. Mousavi and A. Tadaion, "A Simple Two-stage detector for Massive MIMO Systems with one-bit ADCs," in *Proceedings of the 27th Iranian Conference on Electrical Engineering (ICEE)*, Apr. 2019, pp. 1674–1678.

[15] Q. Bai and J. A. Nossek, "Energy efficiency maximization for 5G multi-antenna receivers," *Transactions on Emerging Telecommunications Technologies*, 2015. [Online]. Available: https://mediatum.ub.tum.de/doc/1289834/1289834.pdf

[16] H. N. Dang, T. V. Nguyen, and H. T. Nguyen, "Improve Uplink Achievable Rate for Massive MIMO Systems With Low-Resolution ADCs," in *Proceedings of the 2020 IEEE Eighth International Conference on Communications and Electronics (ICCE)*, 2021, pp. 99–104.

[17] T. Liu, A. Liu, H. Zhang, W. Xu, and H. Lei, "Secrecy Performance Analysis of Mixed-ADC/DAC Cell-Free Massive MIMO in the Presence of Multiple Eavesdroppers," *IEEE Transactions on Communications*, vol. 71, no. 3, pp. 1643–1658, 2023.

[18] H. Wang, Y. D. Zhang, B. Zhang, and J. Wang, "Mixed-ADC Based PMCW MIMO Radar Angle-Doppler Imaging," *IEEE Transactions on Aerospace and Electronic Systems*, 2023.

[19] W. Liu, Y. Li, X. Wu, Y. Han, X. Chen, and H. Zhang, "Massive Access in Extra Large-Scale MIMO With Mixed-ADC Over Near-Field Channels," *IEEE Transactions on Communications*, 2023.

[20] Y. Hu, R. Xie, J. Wu, S. Jin, and H. Li, "Channel Estimation for IRS-Assisted mmWave Massive MIMO Systems in Mixed-ADC Architecture," *IEEE Transactions on Wireless Communications*, 2023.

[21] Y. Chen, Y. Liu, Q. Zhang, L. Li, and X. Cao, "Channel Estimation for IRS-Aided Massive MIMO Systems With Mixed-ADC Architecture," *IEEE Wireless Communications Letters*, vol. 12, no. 5, pp. 851–855, 2023.

[22] Y. Gao, Y. Zhang, J. Yuan, J. Zhang, and W. Zhang, "Channel Estimation for mmWave Massive MIMO Systems With Mixed-ADC Architecture," *IEEE Wireless Communications Letters*, vol. 12, no. 6, pp. 953–957, 2023.

[23] A. Elgabli and T. Y. Al-Naffouri, "Hybrid Low-and Full-Resolution ADCs in Uplink Massive MIMO Systems: Performance Analysis and Deep Learning-Based Detection," *IEEE Transactions on Communications*, vol. 71, no. 5, pp. 2877–2893, 2023.
[24] Y. Zhao, Y. Wei, and Y.-C. Liang, "Detection of Multi-User Signals in Massive MIMO Systems With Mixed-ADC Architecture," *IEEE Transactions on Wireless Communications*, vol. 22, no. 8, pp. 5004–5018, 2023.
[25] J. Thorpe, "Low-density parity-check (LDPC) codes constructed from protographs," *IPN Progress Report*, pp. 42–154, 2003.
[26] M. D. Aksun and E. Arıkan, "LDPC code design for 6G wireless," *IEEE Communications Magazine*, vol. 59, no. 11, pp. 76–81, Nov. 2021.
[27] H. N. Dang, T. V. Nguyen, and H. T. Nguyen, "Improve Uplink Achievable Rate for Massive MIMO Systems With Low-Resolution ADCs," in *Proceedings of the 2020 IEEE Eighth International Conference on Communications and Electronics (ICCE)*, 2021, pp. 99–104.
[28] H. D. Vu, T. V. Nguyen, D. N. Nguyen, and H. T. Nguyen, "On Design of Protograph LDPC Codes for Large-Scale MIMO Systems," *IEEE Access*, vol. 8, pp. 46 017–46 029, 2020.
[29] P. A. Hoeher and T. Wo, "Superposition Modulation: Myths and Facts," *IEEE Communications Magazine*, vol. 49, no. 12, pp. 110–116, Dec. 2011.
[30] J. Luo, Y. Bai, B. Bai, C. Chen, and W. Wen, "A Multilayer Superposition Modulation Scheme to Improve the Data Rate for IoT Communications," in *Proceedings of the 2023 IEEE/CIC International Conference on Communications in China*, Dalian, China, Aug. 2023, pp. 1–6.
[31] D. Hao and P. A. Hoeher, "Superposition Modulation with Reliability-Based Hybrid Detection," in *Proceedings of the 2010 6th International Symposium on Turbo Codes and Iterative Information Processing (ISTC)*, Brest, France, Sep. 2010, pp. 280–284.
[32] Y. H. Choi and S. W. Heo, "A Novel Decoding Algorithm of Superposition Modulation for Cooperative IoT System," in *Proceedings of the 2020 IEEE International Conference on Consumer Electronics (ICCE)*, Las Vegas, NV, USA, Jan. 2020, pp. 1–2.
[33] C. Hasan and U. Aygolu, "An incremental relaying approach for superposition modulated cooperative transmission," in *Proceedings of the 2009 IEEE Wireless Communications and Networking Conference (WCNC)*, Budapest, Hungary, Apr. 2009, pp. 1–6.
[34] X. Lu, T. J. Li, and Y. Liu, "Multiuser Cooperative Transmission Through Superposition Modulation Based on Braid Coding," in *Proceedings of the 2015 IEEE International Conference on Acoustics, Speech and Signal Processing (ICASSP)*, South Brisbane, QLD, Australia, Apr. 2015, pp. 3128–3132.
[35] S. Zhao, X. Ma, and B. Bai, "Decoding Algorithms of LDPC Coded Superposition Modulation," *IEEE Communications Letters*, vol. 18, no. 3, pp. 487–490, Mar. 2014.
[36] M. Srinivasan and S. Kalyani, "Analysis of Massive MIMO With Low-Resolution ADC in Nakagami- *m* Fading," *IEEE Communications Letters*, vol. 23, no. 4, pp. 764–767, Apr. 2019.
[37] H. T. Nguyen, T. A. Ramstad, and I. Balasingham, "Wireless sensor communication system based on direct-sum source coder," *IET Wireless Sensor Systems*, vol. 1, no. 2, pp. 96–104, June 2011.
[38] D. Hui and D. L. Neuhoff, "Asymptotic analysis of optimal fixed-rate uniform scalar quantization," *IEEE Transactions on Information Theory*, vol. 47, no. 3, pp. 957–977, March 2001.
[39] W. Fukuda, T. Abiko, T. Nishimura, T. Ohgane, Y. Ogawa, Y. Ohwatari, and Y. Kishiyama, "Low-Complexity Detection Based on Belief Propagation in a Massive MIMO System," in *Proceedings of the 2013 IEEE 77th Vehicular Technology Conference (VTC Spring)*, June 2013, pp. 1–5.
[40] T. Takahashi, S. Ibi, and S. Sampei, "On Normalization of Matched Filter Belief in GaBP for Large MIMO Detection," in *Proceedings of the 2016 IEEE 84th Vehicular Technology Conference (VTC-Fall)*, Sep. 2016, pp. 1–6.
[41] H. D. Vu, T. V. Nguyen, T. B. Do, and H. T. Nguyen, "Belief Propagation Detection For Large-Scale MIMO Systems With Low-Resolution ADCs," in *Proceedings of the 2019 International Conference on Advanced Technologies for Communications (ATC)*, 2019, pp. 68–73.
[42] T. J. Richardson, M. A. Shokrollahi, and R. L. Urbanke, "Design of capacity-approaching irregular low-density parity-check codes," *IEEE Transactions on Information Theory*, vol. 47, no. 2, pp. 619–637, Feb. 2001.
[43] S. ten Brink, G. Kramer, and A. Ashikhmin, "Design of low-density parity-check codes for modulation and detection," *IEEE Transactions on Communications*, vol. 52, no. 4, pp. 670–678, Apr. 2004.
[44] G. Liva and M. Chiani, "Protograph LDPC Codes Design Based on EXIT Analysis," in *Proceedings of the IEEE GLOBECOM 2007 - IEEE Global Telecommunications Conference*, Nov 2007, pp. 3250–3254.
[45] Y. Fang, P. Chen, L. Wang, F. C. M. Lau, and K. K. Wong, "Performance analysis of protograph-based low-density parity-check codes with spatial diversity," *IET Communications*, vol. 6, no. 17, pp. 2941–2948, Nov. 2012.
[46] T. V. Nguyen and A. Nosratinia, "Rate-Compatible Short-Length Protograph LDPC Codes," *IEEE Communications Letters*, vol. 17, no. 5, pp. 948–951, May 2013.
[47] T. V. Nguyen and H. T. Nguyen, "The design of optimized fast decoding protograph LDPC codes," in *Proceedings of the 2016 International Conference on Advanced Technologies for Communications (ATC)*, Oct. 2016, pp. 282–286.
[48] T. Abiko, W. Fukuda, T. Nishimura, T. Ohgane, Y. Ogawa, Y. Ohwatari, and Y. Kishiyama, "An EXIT Chart Analysis for Belief-Propagation Based Detection in a Large-Scale MIMO System," in *Proceedings of the 2013 IEEE 77th Vehicular Technology Conference (VTC Spring)*, June 2013, pp. 1–5.
[49] H. N. Dang, H. T. Nguyen, and T. V. Nguyen, "Joint Detection and Decoding of Mixed-ADC Large-Scale MIMO Communication Systems With Protograph LDPC Codes," *IEEE Access*, vol. 9, pp. 101 013–101 029, 2021.
[50] H. Uchikawa, "Design of non-precoded protograph-based LDPC codes," in *Proceedings of the 2014 IEEE International Symposium on Information Theory*, Jun. 2014, pp. 2779–2783.
[51] X.-Y. Hu, E. Eleftheriou, and D. M. Arnold, "Regular and irregular progressive edge-growth tanner graphs," *IEEE Transactions on Information Theory*, vol. 51, no. 1, pp. 386–398, Jan 2005.

Duc A. Hoang graduated from Hanoi University of Science and Technology in Vietnam, where he majored in automatic control. He then received a master's degree in aircraft control from the Military Technical Academy. He is currently a graduate student at Posts and Telecommunications Institute of Technology, specializing in telecommunications engineering.

Thang N. Le received his B.Eng. degree in Radio-Electronics and Communication from Hanoi University of Science and Technology (HUST), Vietnam, in 1995; his M.Eng. degree in Telecommunications from the Asian Institute of Technology (AIT), Bangkok, Thailand, in 2000; and his Ph.D. degree in Information and Communication Technology (ICT) from the Department of Computer Science and Telecommunications (DIT), University of Trento, Italy, in 2006. He is currently an Associate Professor and the Dean of the Postgraduate Studies Faculty at the Posts and Telecommunications Institute of Technology (PTIT), Hanoi, Vietnam. His research interests include performance analysis, modeling and simulation, wireless communication systems, physical layer security, queueing theory, and related applications.

Hieu T. Nguyen received his B.Sc., M.Sc., and Ph.D. degrees in Electrical Engineering from Hanoi University of Science and Technology, the University of Saskatchewan (Canada), and the Norwegian University of Science and Technology, respectively. He is currently a faculty member in the Faculty of Technology, Natural Sciences, and Maritime Sciences at the University of South-Eastern Norway (USN).